Eindhoven University of Technology

MASTER

Identification of Spatio-Temporal Models for Overactuated Mechanical Systems

Teurlings, Matthijs H.B.

Award date:
2023

Link to publication

TU/e EINDHOVEN
UNIVERSITY OF
TECHNOLOGY

Graduation Thesis
Project phase

Identification of Spatio-Temporal Models for Overactuated Mechanical Systems

CST 2023.007

Master:	Systems and Control
Department:	Mechanical Engineering
Research group:	Control Systems Technology
Student:	M.H.B. Teurlings
Identity number:	1504274
Thesis Supervisor:	T.A.E. Oomen

Committee members

Chairman:	prof.dr.ir. T.A.E. Oomen
Advisor:	ir. P.J.M.M. Tacx
Member:	dr.ing. I. Cortes Garcia
Member:	dr.ir. L.L.G. Blanken

Eindhoven, 30-Jan-2023

Declaration concerning the TU/e Code of Scientific Conduct for the Master's thesis

I have read the TU/e Code of Scientific Conduct[i].

I hereby declare that my Master's thesis has been carried out in accordance with the rules of the TU/e Code of Scientific Conduct

Date

30-1-2023
....

Name

M.H.B. Teurlings
....

ID-number

1504274
....

Signature

....

Submit the signed declaration to the student administration of your department.

February 21, 2020

Voorwoord

Voor u ligt mijn master thesis over het parametrisch identificeren van complexe mechanische systemen. De thesis dient ter afsluiting van mijn opleiding Systems & Control aan de Technische Universiteit in Eindhoven. Ik heb van mei 2022 tot en met februari 2023 aan het project gewerkt. Het heeft mij de kans gegeven om me te verdiepen in identificatie theorie, waar ik nog veel over wilde leren.

Ik wil graag mijn thesis adviseur Paul bedanken voor zijn begeleiding, coaching, feedback en de waardevolle discussies die we hebben gehad. Zijn inzicht op het gebied van identificatie is erg leerzaam geweest voor mij. Daarnaast wil ik ook Tom, Maurice, Koen en Mike bedanken voor het delen van hun kennis en enthousiasme, wat zeer positief heeft bijgedragen aan mijn afstudeerproject.

Matthijs Teurlings
Eindhoven, January 30, 2023

Abstract

As performance requirements for both speed and accuracy of high-precision mechanical motion stages increase, the flexible behavior that they exhibit can no longer be neglected as it appears in the relevant frequency range for control. Additionally, physical design constraints and classic rigid-body assumptions often limit the number of available spatially distributed sensors and prevent those sensors to measure a performance variable directly, forcing it to be inferred instead. Control techniques that handle this type of inferential problem often require accurate models. The aim of this research is to provide a methodology for accurately identifying spatio-temporal models of overactuated systems which have a limited number of sensors available. A modal approach is pursued that uses prior knowledge to extend the spatial density of available information beyond what would otherwise be possible given the number of available sensors. This information is later interpolated using two different approaches that rely on physical system knowledge and prior knowledge gathered from a finite element analysis, respectively. The resulting spatio-temporal model can be used to estimate a performance variable anywhere within a defined spatial domain. Using two experimental setups, the effectiveness of the proposed sensor extension and interpolation methods is demonstrated.

Contents

Nomenclature

Acronyms

CAD	Computer-Aided Design
DOF	Degree Of Freedom
FEA	Finite Element Analysis
FEM	Finite Element Method
FRF	Frequency Response Function
GP	Gaussian Process
I/O	Input/Output
IDFT	Inverse Discrete Fourier Transform
IFFT	Inverse Fast Fourier Transform
LM	Levenberg–Marquardt
LMFD	Left Matrix Fraction Description
LOOCV	Leave One Out Cross Validation
LPV	Linear Parameter-Varying
LTI	Linear Time Invariant
MIMO	Multiple-Input Multiple-Output
OAT	Over-Actuated Test rig
POI	Point of interest
SK	Sanathanan-Koerner
STPS	Smooth Thin Plate Spline
SVD	Singular Value Decomposition

Common variables

$\mathcal{L}$	Output matrix of a modal model
$\mathcal{R}$	Input matrix of a modal model

Operators

$\in$	In	$x \in Y$ indicates that x occurs in the elements of Y
$\cup$	Union	$X \cup Y$ indicates a set that contains elements of both X and Y
$\subset$	Proper subset	$X \subset Y$ means that X is a subset of Y
$|\cdot|$	Absolute	$|-x|$ yields x
$\mathbb{E}[\cdot]$	Expected value	$\mathbb{E}[X]$ is the expected value of a random variable X
$\arg\min$	Argument of the minimum	$\arg\min_x f(x)$ yields the value of x for which $f(x)$ is minimal
$\min$	Minimum	$\min(X)$ returns the smallest value in the set X
Δ^2	Biharmonic	$\Delta^2 = (\nabla^2)^2$, where ∇^2 is the partial derivative
$\leftarrow$	Relation	$G_{y \leftarrow x}$ indicates a transfer function from x to y
$\vec{e}_y^x$	Unit frame	$\vec{e}_y^x$ indicates a unit length vector in direction y of reference frame x
vec	Vectorization	$\text{vec}(X)$ stacks all data in matrix X columnwise
$[\cdot]_i$	Row evaluation	$[X]_i$ indicates the i-th row of X
$[\cdot]^j$	Column evaluation	$[X]^j$ indicates the j-th column of X
$\cdot^H$	Complex Conjugate transpose	$\begin{bmatrix} x_1 + y_1 i & x_2 + y_2 i \end{bmatrix}^H = \begin{bmatrix} x_1 - y_1 i & x_2 - y_2 i \end{bmatrix}^\top$
I_x	Identity matrix	I_x indicates a x-by-x sized identity matrix

Sets

$\mathbb{C}$	The set of complex numbers
$\mathbb{R}$	The set of real numbers

Chapter 1

Introduction

Stringent performance requirements in next-generation precision mechatronic systems require explicit control of the flexible dynamic behavior. Traditionally, mechatronic systems can be approximated as a rigid body in the frequency range of interest. However, increasingly stringent demands regarding throughput and accuracy require the flexible dynamic behavior to be controlled explicitly.

Applications that require their flexible dynamics to be accurately controlled include adaptive optics in ground-based telescopes [1, 2], and wafer scanners in photolithography machines [3]. These devices in particular contain a large surface area of a single body where the out-of-plane deflection must be controlled with extreme accuracy at a high bandwidth. In case of ground-based telescopes, this is a large deformable mirror that compensates for atmospheric turbulence. In case of a wafer scanner, it is the surface of a wafer as it undergoes optical exposure, during which the wafer is moving at high speeds in the in-plane directions. The wafer and wafer scanner can be seen as a single body that exhibits flexible behavior and thus the system dynamics vary spatially on it. This creates an inferential control problem as the location at which the wafer is exposed cannot be measured directly. The spatial behavior can also no longer be derived from stage geometry, due to the flexible dynamics in the control bandwidth.

The presence of the flexible dynamics within the control bandwidth require them to be controlled with a large number of spatially distributed actuators, i.e. overactuation. Additionally, a number of sensors larger than the number of Degrees Of Freedom (DOF) might also be required to ensure that the control-relevant flexible behavior is observable in the spatial domain. On many systems including the wafer scanner, it is however not possible or practical to place a large number of sensors due to spatial constraints or cost considerations [4]. Sensors that do get placed might also not be at a control-relevant location. Frameworks for handling this type of complex spatio-temporal control problems include inferential control [5] and robust control [6]. Additionally, feedforward approaches for inferential control problems have also been proposed in [7, 8]. All these methods rely heavily on accurate parametric models of the underlying spatio-temporal flexible dynamics.

Approaches to identify parametric spatio-temporal models based on non-parametric data are mentioned in [9], [10] and [11]. The latter is an identification approach that uses the modal-damped mechanical system model to efficiently and accurately identify modal models [12] with large input/output (I/O) dimensions. It manages to reduce model complexity compared to a full Linear Parameter-Varying (LPV) approach [13–15] by using system knowledge i.e. by assuming that the system to be modeled consists of a single moving body and deformations are small. These identification methods often rely on a set of auxiliary sensors that are temporarily mounted to expand the total number of sensors for identification purposes only. This data is then used to construct a model that can predict the dynamic behavior of a performance variable based on a limited number of sensors during normal operation. The above-mentioned approach of adding a calibration step to the identification procedure is not always feasible or practical to implement, nor is it scalable.

Although several approaches to identify the behavior of flexible systems exist, at present, a method that allows accurate spatio-temporal identification of an overactuated flexible body using limited sensors, is not available. The aim of this thesis is to show that by extending the

modal spatio-temporal identification approach in [11] with prior system knowledge based on the Betti-Maxwell reciprocal theorem [16], [17, Sec 9.2] it is possible to identify a modal LPV model using fewer sensors. A key insight that the reciprocal theorem provides is a reinterpretation of the available data in such modal models which allows missing sensor data to be supplemented by information from the actuators. Additionally, two methods will be shown that extend the spatially sampled linear time-invariant (LTI) model to an LPV model that can predict a performance variable anywhere in a relevant spatial domain. The resulting modal model should be able to capture the complex spatio-temporal behavior of the system, thereby enabling model-based control of next-generation motion systems. The research challenge that is addressed in this thesis is thus:

> *Develop a method that exploits prior knowledge of overactuated mechanical systems and enables using fewer sensors whilst still accurately identifying the flexible dynamics in a control-relevant model.*

Three main sub-questions can be derived based on this challenge, namely:

Q1 How can prior mechanical system knowledge be used to increase the spatial resolution of identified models where only a limited set of sensors is available?

Q2 How can a spatially sampled model be extended to provide an estimate of the flexible dynamics anywhere in a spatial domain?

Q3 To what extent is model accuracy affected by potential approaches that deal with a limited sensor set, compared to when a large sensor set is available instead?

The main contributions of this thesis are now listed, note that some contain sub-contributions as well. Here, contributions C1.1, C1.2 and C2 relate to sub-questions Q1, Q2 and Q3, respectively.

C1 Define a systematic approach for identifying spatio-temporal models of mechanical systems by exploiting prior mechanical system knowledge.

C1.1 Formulate a method to combine information from the input and output matrices of an identified modal model to extend mode shape information and thus provide more densely sampled mode shape data than would otherwise be possible given the number of sensors available.

C1.1.1 Provide insight into the physical meaning of the input and output matrices of a modal model.

C1.1.2 Formulate an approach to combine information from these input and output matrices.

C1.1.3 Provide insight into rigid-body mode shape blending.

C1.1.4 Define a method to find optimal locations for placing special collocated sensor and actuator pairs.

C1.2 Define two robust methods for interpolating discretely sampled mode shapes.

C1.2.1 Show mode shape interpolation using the well-known Smooth Thin Plate Spline algorithm.

C1.2.2 Introduce an interpolation method that uses Gaussian Processes and prior system knowledge based on FEM simulations.

C2 Experimentally validate the proposed methods for extending mode shape data and interpolation.

1.1 Considered system class

In this research, the considered systems class of next-generation motion systems, that includes wafer scanners and adaptive optics, is defined by systems where a single flexible body must be

controlled with a large number of spatially distributed actuators. These systems must have high stiffness and predominantly exhibit linear dynamics, meaning low friction, low backlash, and be lightly damped. The performance variable on the flexible body may not coincide with the measured variables and can change location over time. This body must be overactuated, such that flexible behavior can be identified and controlled. The minimal number of sensors should at least be equal to the number of unconstrained DOF of the flexible body. It is also assumed that the in-plane locations at which available sensors and actuators act on the flexible body are constant. The research will focus on flexible bodies that approximate a thin plate or thin beam i.e. bodies where one dimension is significantly smaller than the others. The flexible behavior is considered in the out-of-plane direction of these bodies and the deformations are assumed to be small.

1.2   Thesis outline

The concept of using fewer sensors will be demonstrated on two different experimental setups. The first one, as discussed in section 2.1 is called the Over-Actuated Test rig (OAT) and it emulates part of a wafer stage used for photolithography in chip manufacturing. The second setup is introduced in section 2.2. It is a flexible beam system that is intentionally built to evaluate new identification and control methods for next-generation motion systems. A method to model flexible structures will be provided in chapter 3, along with a general overview of the proposed identification framework. In chapter 4, the method used to retrieve non-parametric measurements from both setups is discussed and an algorithm that is used to fit a parametric modal model to available non-parametric data is provided. In section 5.1, the concept of the reciprocal theorem is applied to modal models and its implications are explained. Contribution C1.1 and its first three sub-contributions about combining sensor and actuator information are treated in section 5.2. In section 5.3, the fourth sub-contribution about the placement of collocated pairs is discussed. Section 5.4 covers contribution C1.2 about mode shape interpolation and in chapter 6 the methods are experimentally verified, constituting contribution C2.

Chapter 2

Problem formulation

To test and validate any solution approaches for identifying spatio-temporal models, two benchmark setups will first be introduced in this chapter. Both systems are overactuated and exhibit flexible dynamics in the control-relevant frequency range, which suits the considered system class. The first setup is the Over-Actuated test rig (OAT) which emulates the short-stroke of a next-generation wafer stage used for photolithography in chip manufacturing. The second setup is the flexible beam system. Contrary to the 2-dimensional spatial domain of the OAT, which relates to out-of-plane deflection, the flexible beam system only has a 1-dimensional spatial domain. In some cases, this makes visualizing and interpreting modal information more intuitive. Both setups will be used to illustrate and verify identification methods. Next, the problem formulation is given.

2.1 The Over-Actuated Test rig

The OAT is a setup created to test new actuator concepts for current 300 mm and next-generation 450 mm wafer stages. The challenge accompanying larger wafer diameters is, apart from accurately positioning in 6-DOF, about identifying and controlling the flexible dynamics related to out-of-plane deflection at a changing point of interest (POI) during dynamic movements of the stage. Here, the POI does not coincide with the measured variables, creating an inferential control problem that requires an accurate spatio-temporal model to be identified.

When large movements and high accuracy are required, the mechanics are often separated into a long stroke and short stroke, which provide coarse and fine positioning, respectively. The OAT setup is depicted in Figure 2.1 and provides the mechanics of the short stroke. Here, a large granite base ⑦ sits on top of a three-legged stiff frame, it provides surfaces for the chuck force frame ⑥, the three air mounts ④, and the scanning sensor slide ⑨. The chuck force frame is used to actuate the chuck or wafer table ⑤ in 6-DOF, i.e. all chuck forces are created relative to this frame. It contains 4 Lorentz actuators to apply forces to the chuck in x-, y-, and R_z-directions,
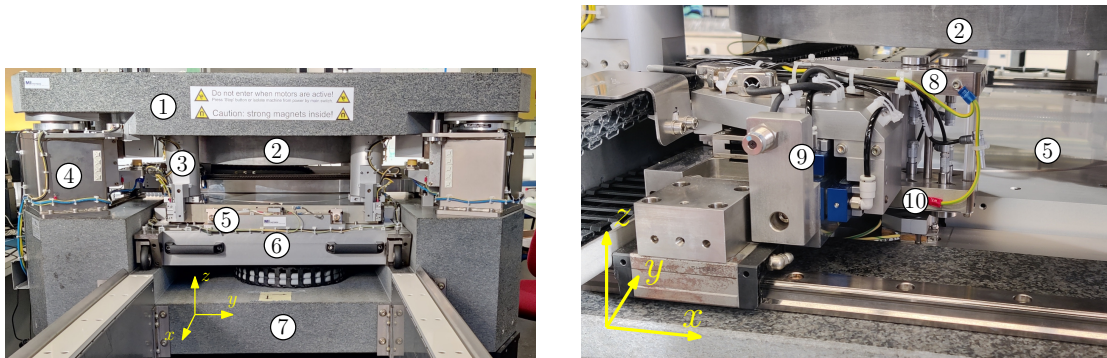
Figure 2.1: Over-Actuated Test rig, with ① Metrology frame, ② Metrology frame reference, ③ one of four pillars attached to the Metrology frame that contains a linear optical encoder for measuring the z-position and may contain in-plane capacitive sensors as well. ④ Air mounts, ⑤ wafer table with dummy wafer, also called the Chuck, ⑥ Chuck force frame which contains all actuators that interact with the Chuck, ⑦ Granite base frame, ⑧ capacitive sensors that measure the reference surface, ⑨ scanning sensor slide, ⑩ capacitive sensors that measure wafer deflection.
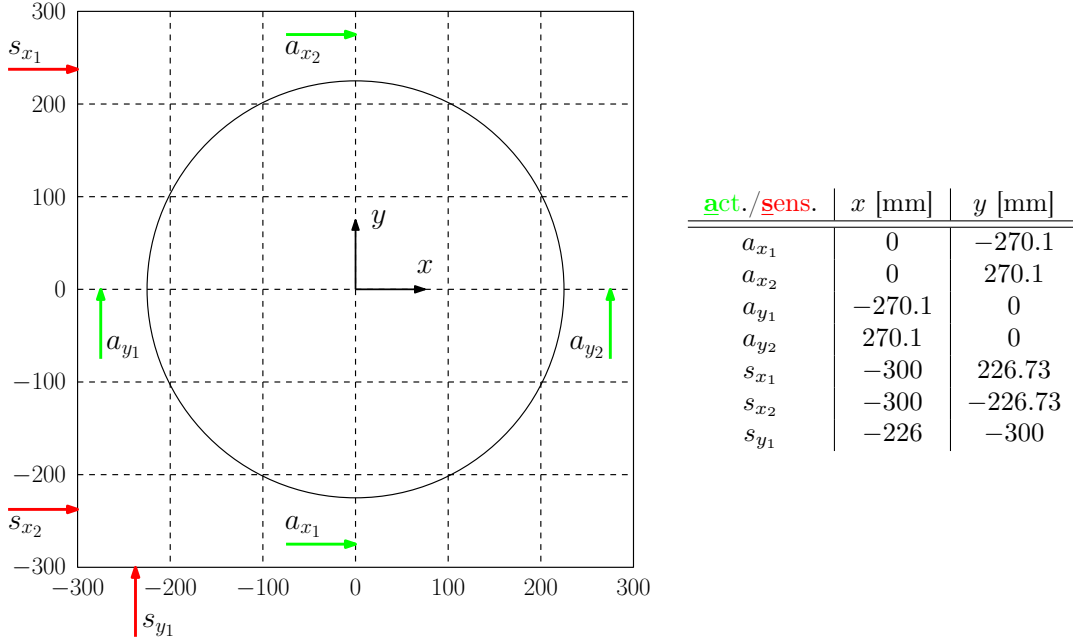
Figure 2.2: Wafer table of the OAT system with locations of actuators ($\rightarrow$) and sensors ($\rightarrow$) in the x- and y-directions.

act./sens.	x [mm]	y [mm]
a_{x_1}	0	−270.1
a_{x_2}	0	270.1
a_{y_1}	−270.1	0
a_{y_2}	270.1	0
s_{x_1}	−300	226.73
s_{x_2}	−300	−226.73
s_{y_1}	−226	−300
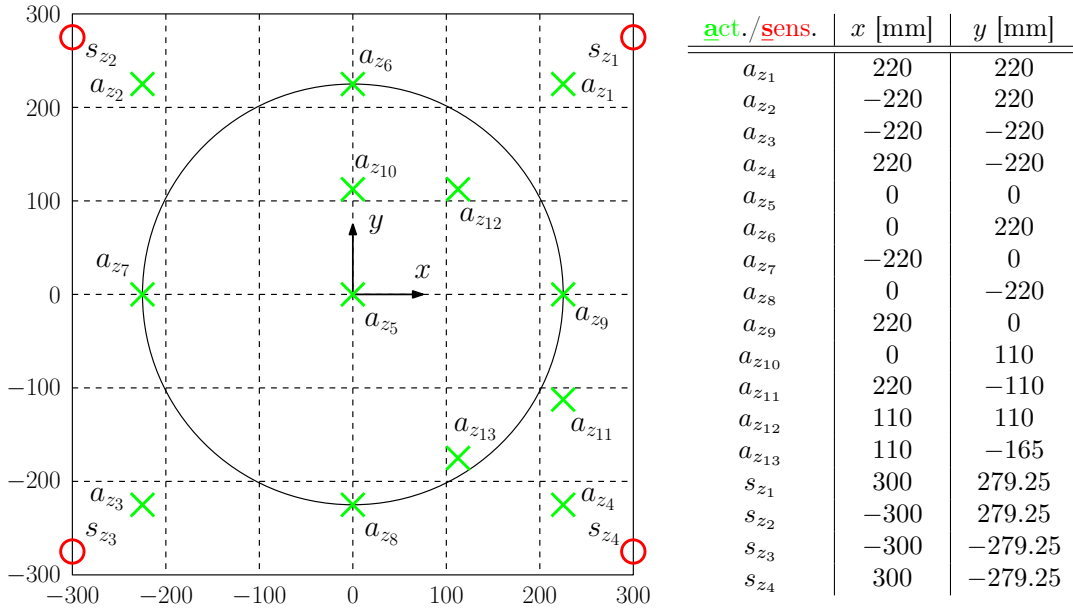
Figure 2.3: Wafer table of the OAT system with locations of actuators ($\times$) and sensors ($\circ$) in the z-direction.

act./sens.	x [mm]	y [mm]
a_{z_1}	220	220
a_{z_2}	−220	220
a_{z_3}	−220	−220
a_{z_4}	220	−220
a_{z_5}	0	0
a_{z_6}	0	220
a_{z_7}	−220	0
a_{z_8}	0	−220
a_{z_9}	220	0
$a_{z_{10}}$	0	110
$a_{z_{11}}$	220	−110
$a_{z_{12}}$	110	110
$a_{z_{13}}$	110	−165
s_{z_1}	300	279.25
s_{z_2}	−300	279.25
s_{z_3}	−300	−279.25
s_{z_4}	300	−279.25

their locations are schematically shown in Figure 2.2. To offset the mass of the chuck, it also contains four gravity compensators in the corners, establishing a mid-air equilibrium in z-direction. Lastly, an equally spaced 9×9 mounting grid is provided in which voice coil actuators for the z-direction can be placed. 13 Of such actuators have been mounted in the current setup, their locations are schematically depicted in Figure 2.3. These actuators facilitate movement in R_x-, R_y-, and z-directions. The OAT is considered to be a next-generation motion stage since it is overactuated, i.e. the number of actuators is larger than the number of DOFs that they constrain,

Figure 2.4: Approximate CAD model of the wafer table. On the left, the top view is displayed, and on the right the bottom view. Note that some details such as (threaded) mounting holes have been left out. The critical dimensions of this approximation are consistent with the actual wafer table as described in [18].

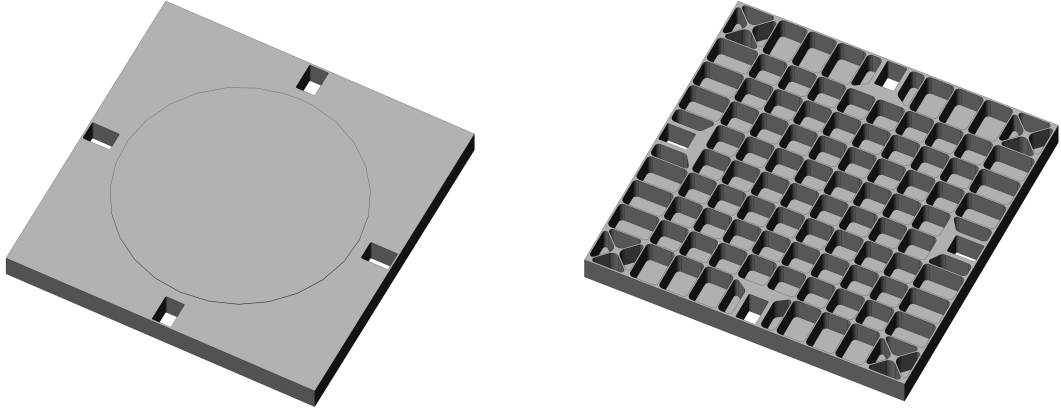enabling control of flexible behavior. On top of the air mounts ④, the metrology frame ① is mounted. All sensor measurements are made relative to this frame. The air mounts have a very low stiffness to prevent disturbances such as ground- or actuator vibrations from influencing the measurements. They are also electronically controlled to ensure alignment with the base frame. Attached to the metrology frame are four pillars, one is marked ③, that each contain an optical encoder to monitor the z-position of the chuck as well as the R_x- and R_y-rotations. Two pillars also contain an additional total of three capacitive sensors to measure the in-plane position i.e. x, y, and R_z. The sensor locations can also be found in figures 2.2, 2.3.

For identifying and verifying the behavior of the flexible dynamics it must be possible to measure the deflection of the chuck in z-direction at many different locations. Instead of adding multiple sensors at set locations, a scanning sensor slide ⑨ is mounted to the base frame. This H-bridge style slide can move to many locations on the wafer table and uses multiple capacitive sensors ⑧, ⑩ to measure the wafer surface and the Metrology frame reference ② simultaneously. By combining these measurements, any disturbances in z-direction created by the sensor slide are compensated for. More information about this setup can be found in [18]. The scanning sensor slide is the ideal tool to verify the quality of identified spatio-temporal models of the OAT. Unfortunately, this hardware was not operational at the time of writing this thesis, so an alternative verification test is later provided.

Figure 2.4 shows the top and bottom view of the chuck. Note that the 9×9 grid of mounting locations is visible in the bottom view along with the gravity compensator mounting locations in each of the four outer corners. A space has also been left for the four in-plane actuators halfway along the edges of the chuck.

2.2   The flexible beam setup

In this section, a general description will be given of a high-precision motion stage that contains a flexible body. The system has no inherent use in a production environment but serves as an analog for many motion systems that exhibit flexible dynamics. It is thus mostly used for evaluating identification and control strategies. In this work, it will be used to verify modal identification methods.

2.2.1 Experimental system

The flexible beam system is depicted schematically in Figure 2.5 and physically in 2.6. The flexible body is a steel beam that has dimensions $2 \times 20 \times 500$ mm and is suspended by 4 vertical wire flexures [19] that constrain translation in z-direction and rotation around the x and y axes. An additional horizontal flexure constrains translation in the x-direction, such that only translation in y-direction and rotation around the z axis is possible. The system thus has two degrees of freedom that each correspond to a rigid-body mode shape. Note that the schematic view does not display any of the wire flexures present in the real system. The constraints are nevertheless similar for small deflections. As can be seen in Figure 2.6, the setup contains 5 fiber optic displacement sensors marked as $x_1, \ldots, x_5$. These sensors observe the distance to the beam. On the opposite side of the beam, three current-driven voice coil actuators are mounted marked F_1, F_3, and F_5. Note that each actuator has a collocated sensor with the same index number $(\cdot)_i$. This number also indicates the normalized physical location of a sensor or actuator. Given that the numbers of actuators and sensors are larger than the number of DOFs, the system is considered overactuated and oversensed. This surplus can be used for identifying and controlling the flexible behavior of the system.

2.2.2 Simulated system

A simulation of the flexible beam system was also made to more efficiently test modal parametric identification methods. The simulation features two additional actuators F_2, and F_4 as shown in Figure 2.5, providing more data for verification purposes. It was created using the Simscape Multibody toolbox in Matlab Simulink. The toolbox is used to define joints between rigid bodies and the fixed world. Because the flexible body of the system is only measured at discrete points, it is modeled as a set of rigid bodies that are connected with revolute joints that have rotational stiffness and damping. The real system is considered stable as the stiffness of the vertical wire flexures limits the deflection in y direction when a force is applied. In the simulated model, these stiffnesses are also implemented. Effects of gravity are disregarded in the simulation.
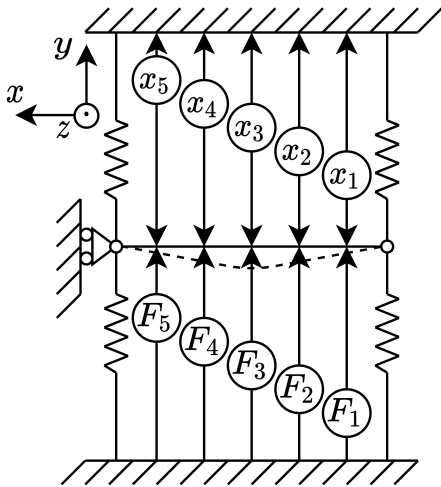
Figure 2.5: Schematic view of the flexible beam setup, note that actuators F_2 and F_4 are not present in the physical setup shown in Figure 2.6.
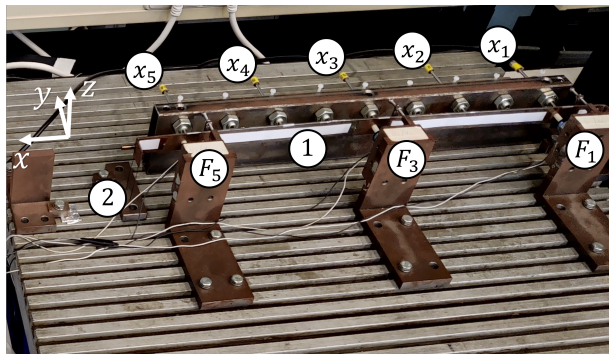
Figure 2.6: Experimental flexible beam setup. Here F_1, F_3 and F_5 mark the locations of three force actuators connected to a beam marked with ①, $x_1, \ldots, x_5$ indicate the locations of 5 fiber-optic sensors observing the distance to the beam. The beam is suspended by wire flexures on both ends marked with ②.

2.3   Problem formulation

Increasingly stringent demands such as a larger wafer diameter, whilst still requiring high performance, are typical for a next-generation motion system such as the OAT. Here, a larger wafer diameter leads to flexible dynamics within the control bandwidth, which causes position-dependent behavior. This requires a large number of spatially distributed actuators to control it. In the considered system class of overactuated next-generation motion systems, which includes the OAT, however, only a limited number of sensors can be placed due to physical constraints. This ensures that the POI, i.e. the wafer exposure location, is not at any of the measured locations, creating an inferential control problem that requires accurate spatio-temporal models to be identified. Current approaches for identifying the spatial aspect of spatio-temporal models are limited by the number of sensors available. They might thus yield insufficient spatial resolution and accuracy for the given system class. The main aim of this thesis is thus to identify accurate spatio-temporal models of overactuated systems that have a limited sensor set, using prior system knowledge of mechanical systems. The approach that is pursued will be outlined in the next chapter.

Chapter 3

Approach to modeling mechanical systems

In this chapter, a modal modeling method is shown that can capture the rigid-body and flexible dynamics of mechanical systems in the relevant system class. Next, an identification approach is formulated that uses this modeling method to identify spatio-temporal models using limited sensors.

3.1 Modeling flexible structures

In the considered system class, the quantity of interest is the out-of-plane deflection of a thin flexible body. Moreover, structural deformations in the surrounding system are assumed to be sufficiently small such that they do not influence the dynamics of the flexible body. Additionally, the in-plane positions of the actuators are assumed fixed relative to the flexible body. The aim of modeling this flexible structure is to identify a model that can estimate the out-of-plane deflection anywhere in the spatial domain of that flexible body, at any moment in time. To this end, consider the out-of-plane deflection to be $\mathfrak{z}(\varrho, t) \in \mathbb{R}$. Here, ϱ represents the in-plane location in the domain $\mathfrak{D} \in \mathbb{R}^2$, at which the deflection is considered at time t. The spatio-temporal behavior of the deflection can be captured in a basis function expansion [20] that separates the spatial and temporal functions

$$\mathfrak{z}(\varrho, t) = \sum_{i=1}^{n_q} w_i(\varrho) q_i(t). \tag{3.1}$$

It is not possible in practice to define the spatial contribution $w_i(\varrho)$ for the infinite number of locations in the spatial domain $\mathfrak{D}$ as this would require infinite sensors. Instead, the deflection in the entire spatial domain is accurately approximated by a finite set of basis functions. Given that the system predominantly behaves linearly, the temporal contribution $q_i(t)$ of the basis function expansion, can be described by a set of second-order ordinary differential equations

$$\mathcal{M}\ddot{q}(t) + \mathcal{D}\dot{q}(t) + \mathcal{K}q(t) = Qu(t). \tag{3.2}$$

Here, the mass matrix $\mathcal{M} \in \mathbb{R}^{n_q \times n_q}$, the damping matrix $\mathcal{D} \in \mathbb{R}^{n_q \times n_q}$ and the stiffness matrix $\mathcal{K} \in \mathbb{R}^{n_q \times n_q}$ form the dynamics of the system. The matrix $Q \in \mathcal{R}^{n_q \times n_a}$ defines how n_a actuators affect the system dynamics. To ensure that the spatial data is distinguishable from the temporal dynamics in the eventual model, a modal modeling approach is pursued. The dynamics in a modal model are defined by the eigenfrequencies that each have a corresponding damping and mode shape. These eigenfrequencies can be found by solving the undamped generalized eigenvalue problem

$$\left[\mathcal{K} - \omega_i^2 \mathcal{M}\right] \phi_i = 0, \quad i = 1, \ldots, n_q. \tag{3.3}$$

Here, ω_i^2 represents the squared undamped resonance frequencies and ϕ_i are the corresponding eigenvectors. The eigenvector set is defined as $\Phi = \begin{bmatrix} \phi_1 & \ldots & \phi_{n_q} \end{bmatrix}$ and the associated mode shapes are parameterized in the basis $W(\varrho) = \begin{bmatrix} w_1 & \ldots & w_{n_q} \end{bmatrix}$. Importantly n_q here represents the number of modes used to describe the system, which can be limited $n_m < n_q$ depending on the desired eventual controller bandwidth. By now applying the transformation $q = \Phi\eta$ the following mass-normalized modal model can be found

$$G_m(\varrho) : \begin{cases} I\ddot{\eta}(t) + \mathcal{D}_m\dot{\eta}(t) + \Omega^2\eta(t) = \mathcal{R}u(t) \\ \mathfrak{z}(\varrho, t) = \mathcal{L}(\varrho)\eta(t). \end{cases} \tag{3.4}$$

Here $\mathcal{D}_m = \Phi^{-1}\mathcal{M}^{-1}\mathcal{D}\Phi$ and $\Omega^2 = \text{diag}\left(\begin{bmatrix} \omega_1^2 & ... & \omega_{n_q}^2 \end{bmatrix}\right)$. The mode shapes are captured in the columns of $\mathcal{L}(\varrho) = W(\varrho)\Phi$ and the fully parameterized input matrix is given by $\mathcal{R} = \Phi^{-1}\mathcal{M}^{-1}Q$. Note that $\mathcal{L}(\varrho)$ is position-dependent, i.e. it is a function of the scheduling variable ϱ and thus the modal description is linear parameter-varying (LPV). Identifying such a model is the main aim of this research, but this cannot be achieved directly given that the available identification data is not continuous in the spatial domain $\mathfrak{D}$. To identify the system mode shapes using available sensors that are positioned at discrete locations, $\mathfrak{z}(\varrho, t) = \mathcal{L}(\varrho)\eta(t)$ in equation (3.4) is first replaced with a spatially sampled equivalent: $\mathfrak{z}_s(t) = \mathcal{L}\eta(t)$ where $\mathcal{L} \approx \begin{bmatrix} \mathcal{L}(\varrho_1) & ... & \mathcal{L}(\varrho_{n_\varrho}) \end{bmatrix}^\top$ with $\mathcal{L} \in \mathbb{R}^{n_s \times n_m}$. Here, n_s is defined as the number of available sensors.

One of the major benefits of the modal parametrization is that the temporal behavior of the system is fully decoupled in the case of modal damping due to $\mathcal{D}_m$ being diagonal. The additional modeling errors that are incurred by making this assumption are usually small for lightly-damped systems. A fully decoupled system in the case of the modal model in (3.4) indicates independently evolving modes.

In practice, the mass-normalized modal model in (3.4) is formed from a more common representation of a modal model given by

$$\hat{G}_m = \sum_{i=1}^{n_m} \frac{R_i}{s^2 + \zeta_i s + \omega_i^2}. \tag{3.5}$$

Here, ζ_i represents the i-th diagonal element of $\mathcal{D}_m$ and $R_i \in \mathbb{R}^{n_s \times n_a}$ are so-called residue matrices [21, 22]. These matrices are over-parameterized as they are formed from a dyadic product between two modal-participation vectors, i.e. $R_i = \phi_{s,i}\phi_{a,i}^\top$. Here, $\phi_{s,i}$ represents the mode shape as observed by the sensors, and $\phi_{a,i}$ contains mode shape information sampled at actuator locations. These residual matrices should thus be rank 1 [23]. Their relation to (3.4) is that $\phi_{s,i}\phi_{a,i}^\top$ for $i = 1, \ldots, n_m$ contains the same information as is stored in matrices $\mathcal{L}$ and $\mathcal{R}$. This key property is what will later warrant the approach in section 5.2.

The challenge is now to firstly estimate an LTI model that consists of parameters in

$$\theta_m = \text{vec}\left(\begin{bmatrix} \mathcal{L}^\top & \mathcal{R} & \bar{\omega}^2 & \bar{\zeta} \end{bmatrix}\right), \tag{3.6}$$

where $\bar{\zeta}$ represents the diagonal entries of $\mathcal{D}_m$. And secondly, to estimate continuous mode-shapes $\mathcal{L}(\varrho)$ based on the spatially sampled $\mathcal{L}$. Note here that the considered system class has a low number of sensors and thus a poor spatial resolution. An identification approach that handles this problem is elaborated on in the next section.

3.2   Identification approach

In this work, a frequency domain approach is pursued and it is conducted in continuous time. The framework for identifying accurate modal models can be separated into four main blocks as displayed in the light blue section of figure 3.1. First, a robust multi-sine procedure is employed to identify non-parametric frequency response functions. The benchmark systems, as described earlier, require different identification procedures. Namely, open-loop and closed-loop. The procedures applicable to each of the systems will be provided. Next, a modal parametric model, of the form (3.4) is fitted to the non-parametric model. A major benefit of this type of model, when applied to lightly-damped mechanical systems, is that it fully decouples the mode shapes that are present. This provides some scaling freedom in the fitted model that is exploited next in order to extend the available sensor set. The resulting gain matching procedure alters the spatial part of the modal model such that the I/O behavior remains equivalent whilst also now allowing data from the input matrix to be combined with data from the output matrix, thus producing a
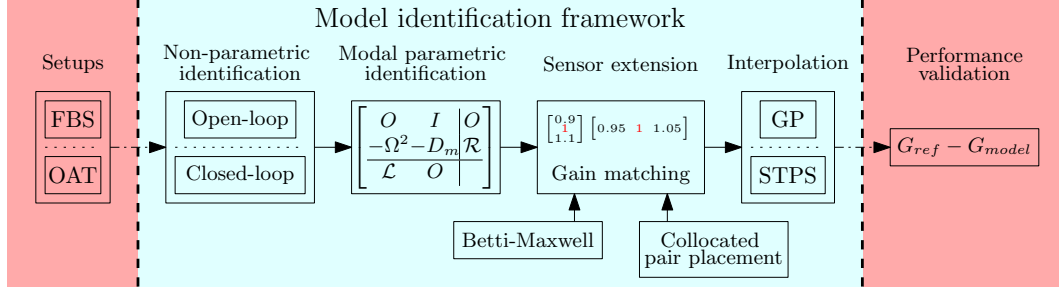
Figure 3.1: Approach to identifying accurate modal mechanical models of overactuated systems that have a limited sensor set

larger spatial resolution of pseudo sensors for each mode shape. The last step in the framework is to interpolate the available sensor data to acquire a model that can provide a sensor estimate at any relevant location. Two different methods have been investigated to achieve this, namely interpolation using Gaussian processes and smooth thin plate spline interpolation.

The two setups, as described, will be used throughout the report to illustrate or demonstrate certain effects that help clarifying the methods used. These will also be used to asses the performance of the proposed framework. In general, the approach here is to provide the identification method with a subset of the available data and then compare model estimates against data that was left out, as a means of validation. The following chapters will provide more detail about each step in the approach.

Chapter 4

Identifying temporal mechanical models

In this chapter, the approach to identify the temporal part of lightly-damped mechanical systems will be described. First, non-parametric identification is discussed which is required for the modal parametric identification that follows.

4.1 Non-parametric identification

To identify a modal parametric model of a flexible mechanical system, first, an accurate non-parametric estimate must be obtained. The flexible beam system can be identified in open-loop as it is stable, but the over-actuated test rig must be identified in closed-loop since the rigid-body modes must be controlled. For all experiments, the identification signals are chosen to be random-phase periodic multi-sines with a flat amplitude spectrum. An advantage of using periodic signals is that no windowing is required, hence no bias errors are introduced as mentioned in [24]. They also lead to more consistent estimates according to [25]. Periodic excitation is beneficial for open-loop as well as closed-loop identification. In [26] such a periodic signal with normalized amplitude spectrum of the form

$$u_0(t) = \frac{1}{\sqrt{N}} \sum_{k=-N/2+1}^{N/2-1} U_k e^{j(2\pi k f_0 t + \phi_k)}, \quad \text{with} \quad f_0 = f_s/N = 1/T \qquad (4.1)$$

is introduced. Here, N is the period length, T is the period time, f_0 is the frequency grid resolution, f_s is the sampling frequency, U_k is the amplitude and ϕ_k is the phase of a particular sine-wave which is chosen as a random variable with a uniform distribution between $[0, 2\pi)$. This formula closely resembles the Inverse Discrete Fourier Transform (IDFT), which makes the generation of such a signal straightforward using the Matlab function `IFFT()` [27]. A full identification signal consists of multiple realizations which each contain multiple periods of a periodic excitation. This reduces disturbing noise as well as stochastic non-linear distortions which yields a smoother measurement. An identification experiment involves injecting an identification signal at an input of the system while measuring an output. The eventual FRF $G(\Omega_k)$ from such an input $u(t)$ to an output $y(t)$ is computed in the frequency domain as

$$G(\Omega_k) = \frac{1}{R} \sum_{r=1}^{R} \frac{\sum_{p=2}^{P} Y_{p,r}(\Omega_k)}{\sum_{p=2}^{P} U_{p,r}(\Omega_k)}. \qquad (4.2)$$
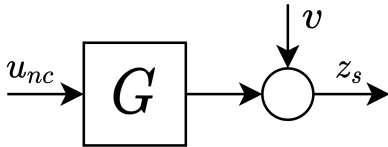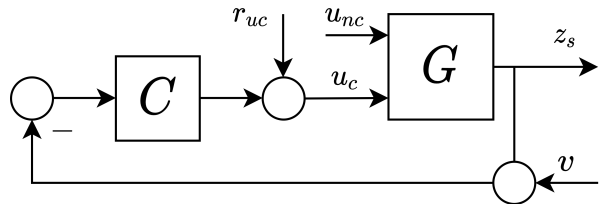

Figure 4.1: Open loop identification scheme

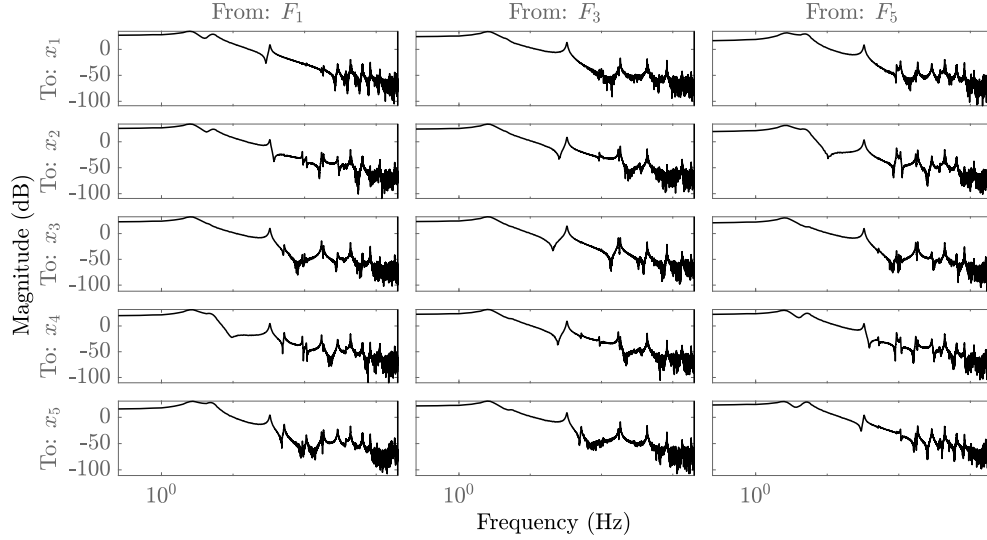Figure 4.2: Closed loop identification scheme

Figure 4.3: Non-parametric estimate of the FRF magnitudes of the experimental flexible beam identification.

Here, P represents the number of consecutive periodic repetitions for every realization $r \in R$. Note that the first period of every new realization is left out to prevent transient behavior from influencing the quality of the eventual FRF. Ideally, the number of periods and realizations is as large as possible since noise will be averaged out more, but this also increases the experiment time which is defined as $t_{exp} = P \cdot T \cdot R$ $[s]$.

Before an FRF is created, the delays imposed by the identification hardware are first determined by visual inspection. This delay is then used to compensate the eventual non-parametric FRF which allows it to be modeled in continuous time.

4.1.1 Open-loop identification

As mentioned, the flexible beam system can be measured in open-loop using the direct approach [28]. Its corresponding identification scheme is shown in Figure 4.1. Here, u_{nc} represents all system inputs, v is the measurement noise and z_s shows the system outputs. A full Multiple-Input Multiple-Output (MIMO) non-parametric FRF model of the system is obtained by separately exciting each actuator whilst measuring all sensors. Equation 4.2 along with the gathered I/O data of each experiment is then used to compute each column of the full system. The identification parameters, as defined in (4.1), are the same for all experiments and are chosen as follows: A sampling frequency of 4096 Hz, a period length of 16384 samples, 10 periods and 10 realizations for a total experiment time of 400 s. Using these settings, a non-parametric identification experiment is now conducted on the experimental flexible beam system. The magnitude plots of the resulting FRF estimates are shown in Figure 4.3. Similar measurements have also been conducted in [29]. In the figure, two rigid-body modes can be observed at 2.5 Hz and 5 Hz. These modes do not occur at 0 Hz since the flexible beam is connected to the fixed world using wire flexures that have a low parasitic stiffness in the direction of actuation. The first flexible mode occurs around 33 Hz.

4.1.2 Closed-loop identification

The rigid-body modes of the OAT system must be controlled to achieve stability. Therefore all identification experiments will be executed in closed-loop. The corresponding identification scheme is shown in Figure 4.2. Note that the approach that will now be discussed is taken from [11] where the same system is identified. Thus, only a brief overview of this method is provided. In Figure 4.2
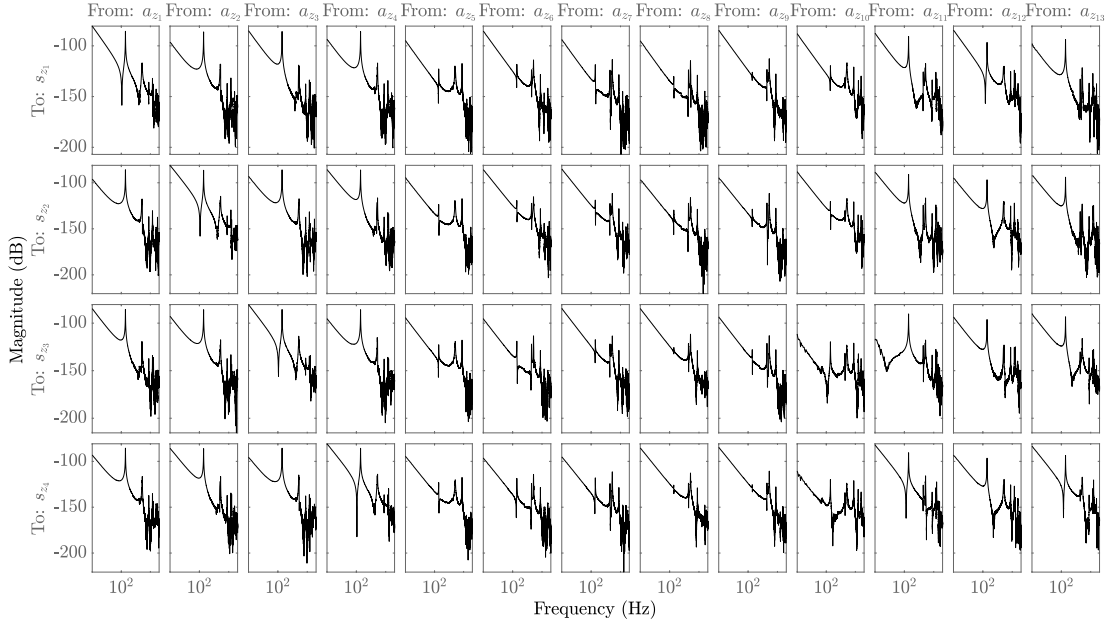
Figure 4.4: Non-parametric FRF magnitudes of the experimental OAT system, courtesy of [31].

a distinction is made between controlled inputs u_c and non-controlled inputs u_{nc}. u_c includes 4 in-plane actuators and 4 out-of-plane actuators. This work aims to identify and control only the out-of-plane deflection and thus, only the out-of-plane actuators in both groups will provide excitation signals for identification. Similarly, only sensors in the set z_s that measure out-of-plane deflection will be considered. The 3-point indirect approach [28] is used to construct the system estimate $\tilde{G}$. The method involves gathering FRF data of the input process sensitivity and input sensitivity function of each I/O pair. The required closed-loop FRF data is thus

$$\tilde{P}_{CL}(\Omega_k) = \begin{bmatrix} \tilde{P}_{z_s \leftarrow r_{u_c}}(\Omega_k) & \tilde{P}_{z_s \leftarrow u_{nc}}(\Omega_k) \\ \tilde{P}_{u_c \leftarrow r_{u_c}}(\Omega_k) & \tilde{P}_{u_c \leftarrow u_{nc}}(\Omega_k) \end{bmatrix}. \tag{4.3}$$

Here $\tilde{P}_{y \leftarrow x}(\Omega_k)$ indicates the relevant transfer function that can be estimated using (4.2) from an input x to an output y at a frequency point Ω_k. The open-loop FRF can be retrieved by multiplying the process sensitivity PS by the inverse of the sensitivity S. This must be the matrix inverse of S and not the element-wise inverse as the latter does not correctly handle interaction in the system [30]. The equation to compute $\tilde{G}(\Omega_k)$ is thus given by

$$\tilde{G}(\Omega_k) = \begin{bmatrix} \tilde{P}_{z_s \leftarrow r_{u_c}}(\Omega_k) & \tilde{P}_{z_s \leftarrow u_{nc}}(\Omega_k) \end{bmatrix} \begin{bmatrix} \tilde{P}_{u_c \leftarrow r_{u_c}}(\Omega_k) & \tilde{P}_{u_c \leftarrow u_{nc}}(\Omega_k) \\ \tilde{P}_{u_{nc} \leftarrow r_{u_c}}(\Omega_k) & \tilde{P}_{u_{nc} \leftarrow u_{nc}}(\Omega_k) \end{bmatrix}^{-1}. \tag{4.4}$$

Note here that $\tilde{P}_{u_{nc} \leftarrow r_{u_c}}(\Omega_k) = \mathbf{0}$ and $\tilde{P}_{u_{nc} \leftarrow u_{nc}}(\Omega_k) = I$ due to the structure in Figure 4.2. Given that any system delays have been compensated for, the rest of the control-relevant parametric identification procedure can be done in continuous time. The resulting non-parametric model of the experimental system that contains the relevant open-loop FRFs is shown in Figure 4.4. In the figure, the names of the input and outputs correspond to those mentioned in Figure 2.3. This system has three rigid-body modes that are all located at 0 Hz since the system has no stiffness to the fixed world in open-loop. The first flexible mode occurs around 139 Hz.

4.2 Parametric identification method

In this section, the optimization problem and a step-wise overview of the algorithm as formulated in [11], used to fit a modal model to Frequency Response Function (FRF) data, is provided. For

brevity, some mathematical details about the exact implementation are left out as they are less relevant to the current research.

The parameters in the vector θ_m defined in (3.6) are minimized by a weighted cost function of the form

$$\hat{\theta} = \arg\min_{\theta} V(\theta) = \sum_{k=1}^{m} \varepsilon\left(s_k, \theta\right)^H \varepsilon\left(s_k, \theta\right), \qquad (4.5)$$

where

$$\varepsilon\left(s_k, \theta\right) = W(k) \, \text{vec}\left(\tilde{G}\left(s_k\right) - \hat{G}\left(s_k, \theta\right)\right), \qquad (4.6)$$

with $W(k) \in \mathbb{C}^{n_s n_a \times n_s n_a}$ being a weighting matrix, s represents the continuous time Laplace variable such that $s_k = j\omega_k$. The cost is thus defined in continuous time as the weighted square sum of differences between the FRF data $\tilde{G}(s_k)$ and $\hat{G}(s_k, \theta)$ which is a (modal) model constructed from parameters in θ. This is a non-linear least squares optimization problem and thus two iterative solving algorithms are employed to find a suitable fit. The approach can be summarized in the following steps.

1) Define the weighting filter $W(k)$. A suitable choice for mechanical systems is to use a Schur weighting filter which has the inverse magnitude of the function to be identified up to a certain frequency range of interest. The reasoning behind this is that mechanical systems often have a -2 slope in their FRF graphs, meaning that higher frequency components have smaller magnitudes and would therefore automatically be weighted less. Additionally, the filter can be customized for a specific system by, for example, emphasizing the accuracy of certain resonance peaks as those define the flexible behavior. This is achieved by clipping the minima of the Schur filter.

2) Formulate the Left Matrix Fraction Description (LMFD) [32] that fits the dimensions of the system to be identified. The LMFD is formulated as

$$\hat{G}(s, \theta) = \hat{D}(s, \theta)^{-1} \hat{N}(s, \theta) \quad \text{with} \quad \hat{N}(s, \theta) \in \mathbb{R}^{n_s \times n_a}[s] \quad \text{and} \quad \hat{D}(s, \theta) \in \mathbb{R}^{n_s \times n_s}[s]. \qquad (4.7)$$

Here, n_s and n_a represent the number of system outputs and inputs, respectively. The two polynomial matrices are linearly parameterized with respect to θ. This parameterization is required as the optimization algorithm in the next step is described specifically for this form.

3) Perform a predetermined number of iterations of the Sanathanan-Koerner (SK) algorithm [33] to reduce the cost function. Then pick the iteration that produced the lowest cost as an initial estimate for the next step. This algorithm generally does not converge to the optimal solution and it also does not do so monotonically. However, it does not require an accurate initial estimate of θ either.

4) Perform a predetermined number of iterations of the Levenberg-Marquart (LM) algorithm [34] given the initial condition produced by the SK algorithm. Unlike the previous algorithm, LM iterations generally converge monotonically at a high rate given a good initial estimate. The sequential use of both algorithms does not guarantee an optimal solution, but will generally yield good results.

5) Perform a transformation from the current LMFD model to an initial estimate of the modal model. This model has the form

$$\hat{G}_m = \sum_{i=1}^{n_m} \frac{R_i}{s^2 + \zeta_i s + \omega_i^2} \quad \text{with} \quad R_i \in \mathbb{R}^{n_s \times n_a}, \qquad (4.8)$$

and is parameterized by (3.6). In this research, all systems are assumed to be modally damped, but modal damping is not enforced in the LMFD parameterization, thus the transformation is not exact. Additionally, the residue matrices R_i for $i = 1, \ldots, n_m$ are separated into the input matrix $\mathcal{R}$ and the output matrix $\mathcal{L}$ using the singular value decomposition (SVD) to arrive at the discretely sampled version of (3.4). More details about this transformation can be found in section 5.2.1.

6) Perform a set of LM iterations to reduce the cost function (4.5), but now given the modal parameterization (4.8) in an attempt to compensate for the non-exact transformation in step 5).

Chapter 5

Identifying spatio-temporal mechanical models

In this chapter, prior knowledge of mechanical systems will be exploited to extend the modal model, as identified thus far, such that its spatial resolution increases. This additional information is then used to more accurately interpolate the mode shapes spatially than would otherwise be possible given the number of available sensors.

5.1   Prior mechanical system knowledge

As shown in section 3.1, the out-of-plane deflection $\mathfrak{z}_s$ for each mode shape is spatially sampled at discrete locations over the physical domain of a flexible body. These locations correspond to physical sensor positions and thus the number of unique mode shapes and their resolution that can be identified is linked to the available number of sensors. One of the goals of this research is to use fewer sensors than would normally be required and still obtain an accurate spatio-temporal model. The Betti-Maxwell reciprocal theorem can be used to reinterpret the available I/O data which will help to extend the number of available sensors with 'pseudo' sensors located at actuator positions. An example of this reciprocal principle is provided in the next section. The concept of reinterpreting data is often used for damage detection in civil engineering applications where instead of using a large number of sensors to identify a structure, manual excitation at many known locations is used while only a small number of sensors are required to register the response, see e.g. [35–37].

5.1.1   Reciprocal theorem applied to motion systems

Consider a 2-mass-spring-damper system as depicted in Figure 5.1 alongside its MIMO FRFs in Figure 5.2. This system can be viewed as an isolated subsection of a larger flexible body. Here, the force F_1 acts on point mass m_1 whose position is defined relative to the fixed world as x_1, the same holds for the second mass. The actuators and sensors are thus collocated. Having minimal sensor data available is emulated by only providing access to $x_1(t)$, $F_1(t)$, and $F_2(t)$. Using this
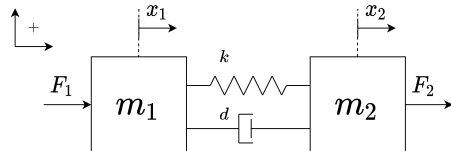

Figure 5.1: 2-mass-spring-damper model. The force F_1 acts on point mass m_1 whose position is defined relative to the fixed world as x_1, the same holds for the second mass.
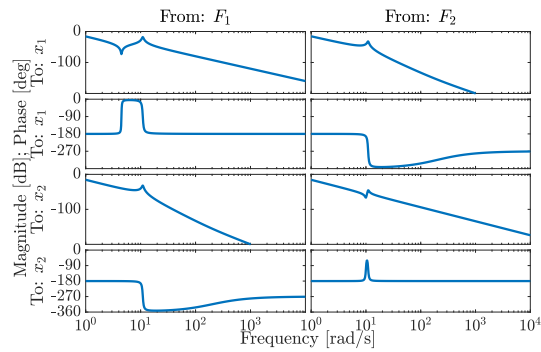

Figure 5.2: Bode plot showing a typical theoretical frequency response functions of the model in Figure 5.1, from inputs F_1 and F_2 to outputs x_1 and x_2.

data and a proper non-parametric identification approach [38], only the top row of FRF plots in Figure 5.2 can be retrieved. The Betti-Maxwell reciprocal theorem [39] states,

Theorem 1. *Consider the system as given by Figure 5.1. If a force F_2 applied to m_2 causes deflection x_1, then that same force applied to m_1 will cause the same deflection at x_2.*

In case sensors and actuators are collocated, as in the example, the transfer function from $F_2 \to x_1$ is equivalent to that from $F_1 \to x_2$, which is indeed the case as demonstrated in Figure 5.2. This example also extends to systems that contain some non-collocated actuators. Indeed, imagine that sensor x_2 does not exist, then the same relation through the collocated pair F_1, x_1 still applies. The concept of extending the sensor set can thus be applied as long as there is at least one collocated sensor and actuator pair. In the modal modeling approach, this interpretation can be used to extend the output matrix $\mathcal{L}$ with data from the input matrix $\mathcal{R}$, allowing to potentially identify more mode shapes. It should be noted however that the modal model is mass normalized and thus there exists a scaling between modes in the input and output matrices. Additionally, some conditions apply to the location of the collocated sensor pairs. Both concepts will be further elaborated upon in section 5.2.

5.2 Actuator and sensor gain matching

In this section, the result of the modal fitting algorithm is interpreted. By recognizing the relationship between data from the input and output matrices in the model, an approach is proposed that extends mode shape resolution.

5.2.1 Interpretation of modal participation matrices

As mentioned in section 3.1, the residual matrices R_i are theoretically rank 1. However, the fitting algorithm, as described in section 4.2, does not enforce this rank condition, but it is re-obtained afterwards using the singular value decomposition (SVD). This function produces unit-length direction vectors U_i and V_i^H, along with corresponding singular values S_i, such that R_i can be decomposed into $U_i S_i V_i^H$. The vectors in U_i and V_i^H associated with the largest singular value in S_i are defined to be the output- and input-vectors for that particular mode i in the modal participation matrices $\mathcal{L}$ and $\mathcal{R}$, respectively. To ensure that the gain from input to output of a particular mode is scaled correctly, the output vectors U_i are multiplied by their maximum singular values S_i. The modal participation matrices are thus defined as,

$$[\mathcal{L}]^i = [U_i]^1 [S_i]_1^1, \quad [\mathcal{R}]_i = [V_i^H]_1, \quad i = 1, \ldots, n_m, \tag{5.1}$$

where $[X]^j$ denotes the jth column and $[X]_k$ denotes the kth row of a matrix X. This method of separating the residual matrix will generally yield good results when the considered system can be accurately modeled as a modal-damped mechanical system [11].

The physical interpretation of the modal participation matrices $\mathcal{L}$ and $\mathcal{R}$ is that they describe what each mode shape looks like, sampled at the locations of either the sensors or the actuators, respectively. In the case of a collocated system, these matrices should thus contain similar data because the physical locations of the actuators are equal to those of the sensors. This theory is demonstrated in the next section.

5.2.2 Similarities in modal participation matrices

FRF data of the 5-by-5 collocated flexible beam system as discussed in section 2.2.2 will now be used to demonstrate similarities between $\mathcal{L}$ and $\mathcal{R}$. To this end, a modal fit was made on that system using the algorithm described in section 4.2 to arrive at a modal decomposition of the form (3.4). Within this section, the following settings have been used for the fitting algorithm.
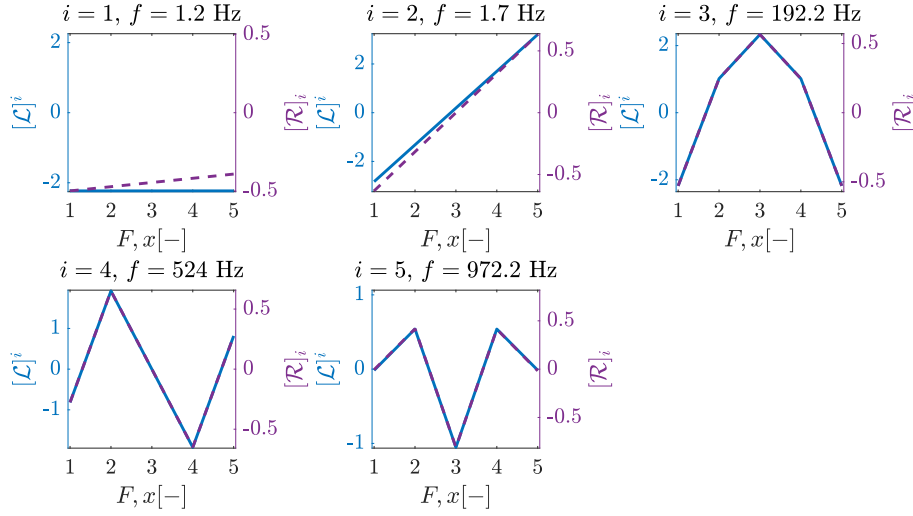
Figure 5.3: I/O mode shapes of a simulated collocated 5-by-5 flexible beam system on which a modal fit was made. Each graph depicts a row of the input matrix $\mathcal{R}$ and a column of the output matrix $\mathcal{L}$ that correspond to mode i.

Modal identification settings. The weighting filter $W(k)$ is chosen to be inverse Schur-weighting with a magnitude cut-off. This ensures all frequencies inside the frequency range of interest are weighted equally. Due to the -2 slope in the magnitude plots of the system, frequencies outside this cut-off are automatically weighted less. Additionally, the minima of this weighting were clipped to emphasize accuracy around resonant frequencies. The LMFD is identified with 30 iterations of the SK-algorithm and refined with 10 iterations of the LM-algorithm. The model is then transformed to a mechanical model and an additional 10 iterations of the LM-algorithm are performed to improve the fit of this model further.

The fitted matrices $\mathcal{L}$ and $\mathcal{R}$ are displayed in Figure 5.3. Here, the columns of $\mathcal{L}$ and the rows of $\mathcal{R}$ that correspond to modes $i = 1, \ldots, n_m$ are each plotted in a separate graph. It is clear from the figure that the rows of $\mathcal{R}$ indeed contain similar mode shape information as the columns of $\mathcal{L}$ apart from a scaling due to $[S_i]_1^1$ in (5.1). Note that there is some dissimilarity for the first two rigid-body modes i.e. $i = 1$ and $i = 2$ due to a slight linear blending between these modes, the level of which is different for the input and output matrix. In contrast, all flexible modes are fully decoupled. This similarity between input and output matrices for collocated systems will be exploited next.

5.2.3 Gain matching using collocated pairs

The separation of the residual matrices R_i into the input and output vectors $[\mathcal{R}]_i$ and $[\mathcal{L}]^i$ is somewhat arbitrary. Indeed, the singular values that have been multiplied by $[U_i]^1$, could have been multiplied with $[V_i^H]_1$ instead. Ideally, both the input- and output matrix are scaled in such a way that they are equivalent when each sensor is collocated with an actuator. This way, systems that have some collocated sensors and actuators could benefit from improved extrapolation quality by

- Scaling the input matrix $\mathcal{R}$ and the output matrix $\mathcal{L}$ using the collocated pairs.

- Extending the output matrix $\mathcal{L}$ with mode shape information from the non-collocated inputs in $\mathcal{R}$.

This way, the total number of points n_z from which mode shape extrapolation is performed can be calculated as

$$n_z = n_s + n_a - n_c, \tag{5.2}$$

where n_c is the number of collocated actuator and sensor pairs. The number of observable points n_z is associated with the number of identifiable mode shapes. In the case of the 5-by-5 flexible beam system, the 5 sensors are placed such that 5 unique mode shapes can be identified. Though, this relation does not hold in general as sensor placement also influences mode shape identification quality. For example, if all sensors are placed close together, then the entire spatial behavior of the flexible beam cannot be determined accurately without making assumptions about symmetry. Given that collocated pairs exist in a system, the following formula can be applied to each identified mode for gain matching the input- and output matrices

$$R_i \approx [\mathcal{L}]^i \frac{1}{\alpha_i} \cdot \alpha_i [\mathcal{R}]_i, \quad \{\alpha_i \in \mathbb{R} | \alpha_i > 0\}, \tag{5.3}$$

In case multiple inputs and outputs are collocated, the optimal α_i is the value that brings the data in $[\mathcal{L}]^i$ and $[\mathcal{R}]_i$, that relates to each collocated pair, the closest together. It can be found by solving the following optimization problem

$$\alpha_i = \arg \min_{\alpha_i \in \mathbb{R}_{>0}} \mathcal{V}_i(\alpha_i), \quad \mathcal{V}_i = \sum_{m=\mathcal{C}(0)}^{\mathcal{C}(n_c)} ([\mathcal{L}]_m^i \frac{1}{\alpha_i} - \alpha_i [\mathcal{R}]_i^m)^2. \tag{5.4}$$

It should be noted that for α_i to have a meaningful value for a particular mode, at least one of the collocated sensor- and actuator pairs should not be located on a knot of that mode. Failing to satisfy this requirement will cause α_i to be undefined. A closed-form solution to the constrained non-linear optimization problem (5.4) can be found by setting the derivative of $\mathcal{V}_i$ to zero as shown below

$$0 = \frac{d}{d\alpha} \sum_{m=\mathcal{C}(0)}^{\mathcal{C}(n_c)} \frac{([\mathcal{L}]_m^i)^2}{\alpha_i^2} + \alpha_i^2 ([\mathcal{R}]_i^m)^2 - 2[\mathcal{L}]_m^i [\mathcal{R}]_i^m,$$

$$0 = \frac{-2 \sum_{m=\mathcal{C}(0)}^{\mathcal{C}(n_c)} ([\mathcal{L}]_m^i)^2}{\alpha_i^3} + 2\alpha_i \sum_{m=\mathcal{C}(0)}^{\mathcal{C}(n_c)} ([\mathcal{R}]_i^m)^2, \tag{5.5}$$

$$\alpha_i = \sqrt[4]{\frac{\sum_{m=\mathcal{C}(0)}^{\mathcal{C}(n_c)} ([\mathcal{L}]_m^i)^2}{\sum_{m=\mathcal{C}(0)}^{\mathcal{C}(n_c)} ([\mathcal{R}]_i^m)^2}}.$$

5.2.4 Retrieving mode shapes from a reduced modal model

The simulation results shown in Figure 5.3 have been created from a 5-by-5 system. Such a system thus has 5 actuators and 5 sensors for a total of 10 devices. Using the scaling method outlined (5.3) it should be possible to retrieve the same modal information using only 6 devices with one collocated pair. This would be computationally cheaper and could reduce system cost. A secondary simulation will now be shown where only the first 4 out of 5 actuators and only 2 out of 5 sensors are used. As mentioned, the location of the collocated pair should be such that no mode ever has a knot at its location. Thus, location 2 is used. The other sensor is placed at location 5. Note that sensor and actuator locations for this system have been defined in section 2.2.1. Figure 5.4 shows the five mode shapes as also featured in Figure 5.3, but now these modes have been constructed from the aforementioned 2-by-4 system. The red and green markers in each of the plots indicate whether mode shape information at a particular location was either gathered from the input matrix $\bar{\mathcal{R}}$ or from the output matrix $\bar{\mathcal{L}}$. The output matrix $\mathcal{L}$ originating from the 5-by-5 system as shown in Figure 5.3 is also plotted in each graph for comparison purposes. The flexible modes, i.e. $i = 3, 4, 5$, correspond well with their reference mode shapes. However, due
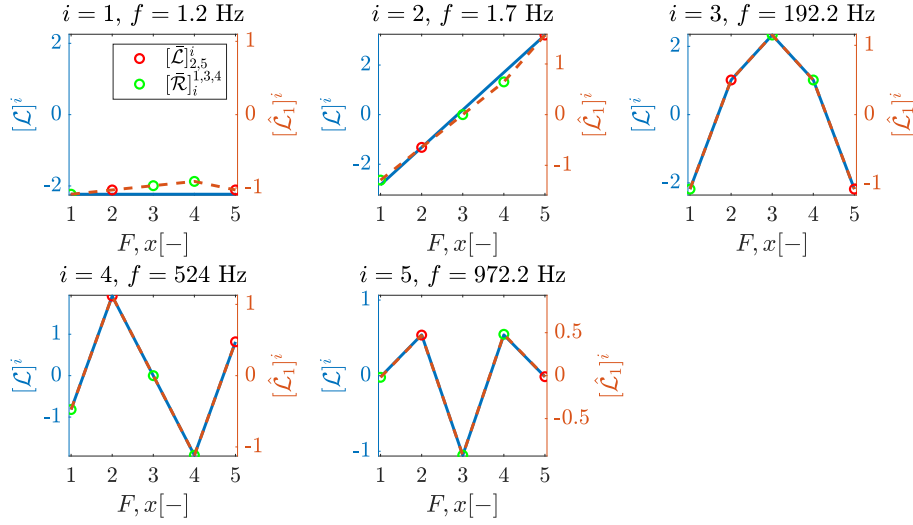
Figure 5.4: Comparison between the modes in output matrix $\mathcal{L}$, of the 5-by-5 system as also featured in Figure 5.3, and the the output matrix $\hat{\mathcal{L}}_1$ which is constructed from elements in the input matrix $\bar{\mathcal{R}}$ and output matrix $\bar{\mathcal{L}}$, i.e. $\hat{\mathcal{L}}_1 \subset (\bar{\mathcal{R}} \cup \bar{\mathcal{L}})$. These matrices belong to an identified modal model of the flexible beam system, where only the first 4 inputs are available as well as outputs 2 and 5.

to blending between the rigid-body modes, the first two modes, i.e. $i = 1, 2$, no longer follow a straight line as would be expected. It will later be shown that this mismatch between gradients of the rigid-body modes in $\bar{\mathcal{L}}$ and $\bar{\mathcal{R}}$ does cause the identified frequency response graphs to be distorted.

5.2.5 Cause of rigid-body mode blending

To elaborate on the effect of rigid-body mode blending, a distinction is made between two effects that it has on modal identification.

1. An identified rigid-body mode shape does not necessarily purely translate or rotate around a predefined coordinate system.

2. A rigid-body mode shape identified on a collocated system may have a difference in gradients between the input matrix $\mathcal{R}$ and the output matrix $\mathcal{L}$.

The cause of both effects can be attributed to the fitting method, more specifically the fitting of the residual matrices R_i as outlined in step 5 of section 4.2. When these residual matrices are fitted, the rank 1 condition is not enforced meaning it is possible that some information is lost when the maximum singular value decomposition is used to retrieve the input and output matrices, as described at the start of section 5.2.1. Moreover, no constraints are placed on the direction vectors U_i and V_i^H themselves, which means that no standard coordinate system is enforced. The effect of this is demonstrated using a mechanical model of a point mass as shown in Figure 5.5. Here, the mass is actuated in two orthogonal directions that align with respect to the $\bar{e}^0$ reference frame. The corresponding state space model is given by

$$G = \left[\begin{array}{c|c} A & B \\ \hline C & \end{array} \right] = \left[\begin{array}{cc|c} 0 & I_2 & 0 \\ 0 & 0 & \frac{I_2}{m} \\ \hline I_2 & 0 & \end{array} \right], \tag{5.6}$$

where I_2 indicates a size 2 identity matrix. Note that this model is already in modal form. A corresponding 2×2 system of non-parametric FRF data is now generated. When this data is
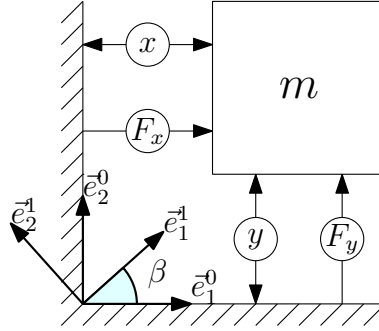
Figure 5.5: Schematic model of a point-mass that is measured and actuated in two orthogonal directions

provided to the unrestricted modal fitting algorithm, it could arbitrarily choose its reference frame as $\vec{e}^1$. The input and output matrices would then become

$$\hat{B} = BM, \quad \hat{C} = M^{-1}C \quad with, \quad M = \begin{bmatrix} \cos(\beta) & \sin(\beta) \\ -\sin(\beta) & \cos(\beta) \end{bmatrix}, \tag{5.7}$$

which explains how rigid-body mode blending as described by effect 1 can occur. Note that both systems would still produce the same FRFs, as they are different modal realizations of the same system. Due to the non-uniqueness of the modal model and lack of constraints between the input and output vectors, it would in fact also be possible to have a difference between these vectors, which explains effect 2. To elaborate further on why this is possible, consider the modal representation of (5.6) given by

$$G_m = \frac{R_1}{s^2} + \frac{R_2}{s^2} = \frac{R_{rb}}{s^2} \Rightarrow \frac{\begin{bmatrix} \frac{1}{m} & 0 \\ 0 & 0 \end{bmatrix}}{s^2} + \frac{\begin{bmatrix} 0 & 0 \\ 0 & \frac{1}{m} \end{bmatrix}}{s^2} = \frac{\begin{bmatrix} \frac{1}{m} & 0 \\ 0 & \frac{1}{m} \end{bmatrix}}{s^2}. \tag{5.8}$$

Here, the rigid-body mode shapes, as represented by the rank one numerators, are separated according to the directions of the $\vec{e}^0$ reference frame. Notice that the denominators are equivalent and thus it is possible to combine these matrices into a rank 2 matrix, e.g. R_{rb}. This structure provides freedom to choose the direction vectors for each mode shape somewhat arbitrarily. As an example, the input and output vectors that form R_1 can also be chosen as $\hat{R}_1 = \begin{bmatrix} \frac{1}{2}\gamma_1 & \gamma_1 \end{bmatrix}^\top \begin{bmatrix} \gamma_1 & \gamma_1 \end{bmatrix}$. A product of two vectors can have a maximum rank of one. To ensure the system response remains the same, each residual matrix must thus remove one rank from R_{rb}. To this end, γ_1 may be computed by solving $\det(R_{rb} - \hat{R}_1(\gamma_1)) = 0$. The vectors that form the secondary rigid-body mode $\hat{R}_2$ are now computed by taking the SVD of $R_{rb} - \hat{R}_{1,\gamma_1}$. The resulting structure is $\hat{R}_2 = \begin{bmatrix} -\gamma_2 & \gamma_2 \end{bmatrix}^\top \begin{bmatrix} -\gamma_2 & \frac{1}{2}\gamma_2 \end{bmatrix}$. A numerical example of (5.8) in case $m = 1$ is provided in (5.9). It shows that there are multiple ways to define the same rigid-body mode shapes and that it is indeed possible to have a difference between input and output vectors for each mode shape.

$$G_m = \frac{\hat{R}_1}{s^2} + \frac{\hat{R}_2}{s^2} = \frac{R_{rb,m=1}}{s^2} \Rightarrow \frac{\begin{bmatrix} \frac{1}{3} & \frac{1}{3} \\ \frac{2}{3} & \frac{2}{3} \end{bmatrix}}{s^2} + \frac{\begin{bmatrix} \frac{2}{3} & -\frac{1}{3} \\ -\frac{2}{3} & \frac{1}{3} \end{bmatrix}}{s^2} = \frac{\begin{bmatrix} 1 & 0 \\ 0 & 1 \end{bmatrix}}{s^2} \tag{5.9}$$

A more general description that defines the set of possible rigid-body mode shapes based on a given matrix such as R_{rb} is given in appendix C. Here, the input and output matrices are assumed to contain the same information.

Since the number of rigid-body modes in the above-given example is two, they can be described by just two parameters γ_1, γ_2, and the structure of one of the modes. Enforcing one or more of the rigid-body mode shapes, in regard to fitting algorithms, reduces the number of parameters and

imposes certain constraints. It is potentially inaccurate to impose the same constraints after an unconstrained fitting algorithm has produced certain input and output vectors, since the desired structure might not fit the identified residual matrices well, causing the resulting fit to be worse. In case of the flexible beam system, as described thus far, the two rigid-body modes actually do not occur at exactly the same 0 Hz frequency since the flexible body is suspended by wire flexures that are connected to the fixed world. Therefore, rigid-body modes are defined as whole-body rotations or translations rather than in-body deformations. Since mode blending still seems to occur between the rigid-body modes of the flexible beam system, an approach that imposes constraints a posteriori is bound to be inaccurate for this system as well.

Flexible modes are not significantly affected by mode shape blending as can be seen in Figure 5.3. This can be attributed to the fact that the flexible modes are much more distinct and thus the fitting algorithm is much more likely to find a unique solution for them. The flexible modes are usually also spaced apart more in the frequency domain, making any mixing between them significantly less likely.

Directly fitting input and output vectors with certain constraints on their directions cannot easily be implemented in the current modal modeling framework as some of the algorithms used, like SK and LM iterations, would become incompatible. In the current research, it is not essential that the rigid-body mode shapes are defined relative to a given reference frame, but a difference between the input and output vectors for identified rigid-body modes will cause inaccuracies when attempting to combine information from both. As such, the next section will provide an ad-hoc solution to this problem which will be demonstrated on the simulated flexible beam system.

5.2.6   Solution to mode blending

Given that at least two sensors are available, the two rigid-body modes of the 2-DOF flexible beam system, can be uniquely identified and linearly extrapolated to other locations without the need for additional information from the input matrix. Note that the sensor locations should be sufficiently far apart on a real system, such that sensor noise and quantization errors influence the rigid-body mode shapes the least. Figure 5.6 shows the same graphs as in Figure 5.4, but now the rigid-body modes are extrapolated based only on the output matrix $\bar{\mathcal{L}}$. As can be seen in the figure, all modes now correspond to those found in the output matrix of the 5-by-5 system, apart
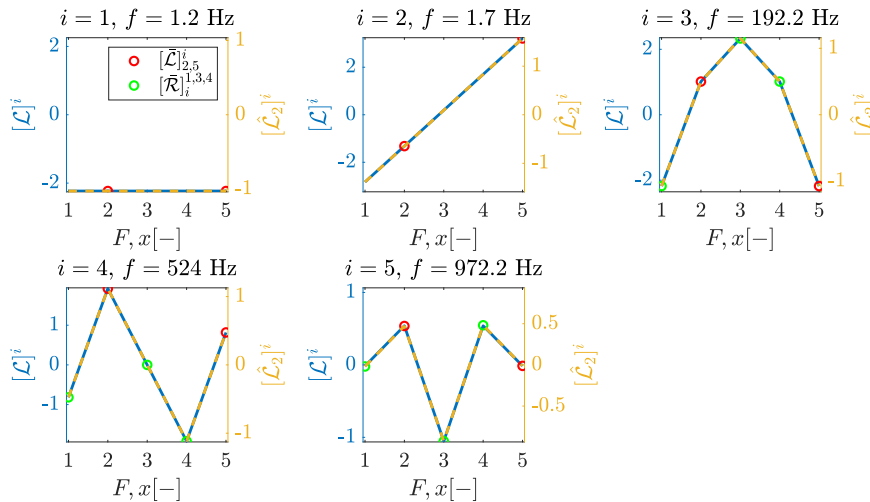

Figure 5.6: The same description as was given in Figure 5.4 applies here as well, with the exception that now the rigid-body mode shapes have been linearly extrapolated based only on the data in $\bar{\mathcal{L}}$ such that $[\hat{\mathcal{L}}_2]^{1,2} \subset [\bar{\mathcal{L}}]^{1,2}$.
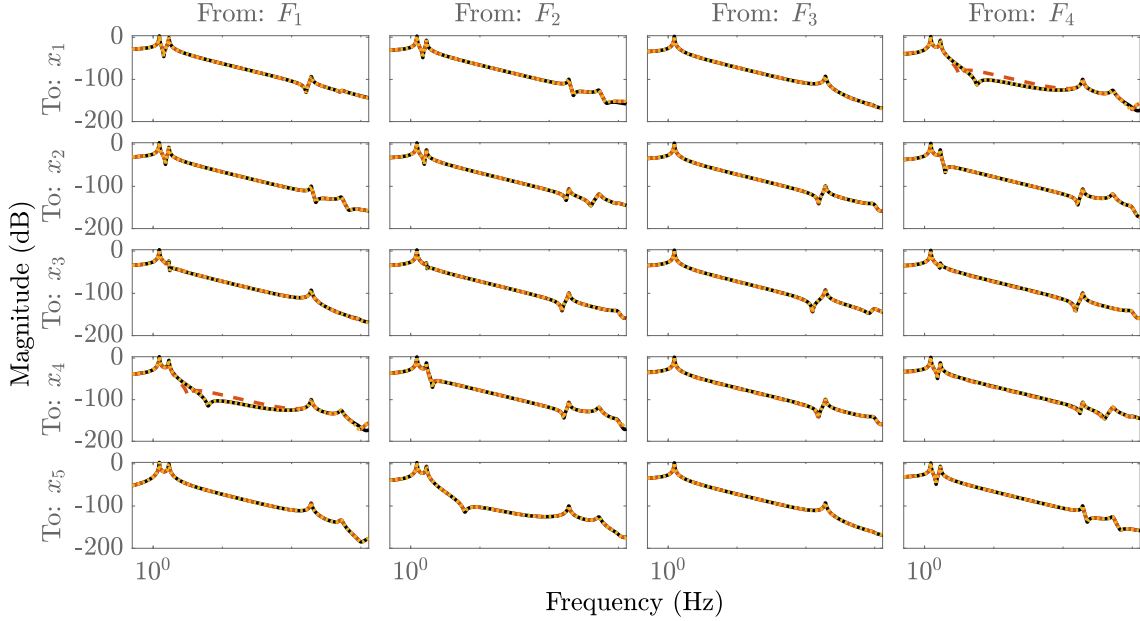
Figure 5.7: Bode diagram that shows the transfer functions from the first 4 inputs to all 5 outputs of the flexible beam simulation. Here, (–) is the FRF data of the simulated system which serves as a reference, (–) is the FRF of the modal model whose output matrix is shown in Figure 5.4, (–) is the FRF of the modal model whose output matrix is shown in Figure 5.6.

from a difference in scaling, which is caused by α and is already compensated for with the input matrix. Two modal systems of the form (3.4) are now constructed. The first one having output matrix $\hat{\mathcal{L}}_1$ from Figure 5.4 and the second having output matrix $\hat{\mathcal{L}}_2$ from Figure 5.6. The modal models are shown in Figure 5.7 along with a reference model. In graphs $F_4 \rightarrow x_1$ and $F_1 \rightarrow x_4$, it is shown that linearly extrapolating the rigid-body modes based only on the output matrix indeed creates a better fit compared to when the input matrix is used instead of extrapolation. The same observation can be made when more closely observing the second mode in graphs: $F_1 \rightarrow x_3$ and $F_2 \rightarrow x_3$.

In conclusion, a smaller number of sensors and actuators, than would generally be required, have been used to construct output vectors $[\hat{\mathcal{L}}_2]^i$ for modes $i \in 1, \ldots, n_m$. These can now be combined to form the columns of the spatially sampled output matrix $\hat{\mathcal{L}}$. In section 5.4, two algorithms are shown that can interpolate this type of matrix to form a continuous estimate for each mode shape in a spatial domain. This is defined in section 3.1 to be $\mathcal{L}(\varrho)$. Note that the flexible beam system used here, has only 1-DOF in its spatial domain, but the methods discussed freely extend to systems that have a 2-DOF spatial domain, such as the OAT system.

5.3   Placement of collocated pairs

As mentioned in section 5.2.3, the locations of the collocated sensor and actuator pairs must be such that for each mode, at least one pair is not located on a nodal line. The largest improvement in modal extrapolation quality can however be achieved when only one sensor and actuator are collocated, such that a larger point cloud can be used for extrapolation according to (5.2). This section will thus focus on finding the optimal location to place a single collocated pair given the expected mode shapes up to a certain frequency range of interest.

The proposed method will be explained for systems that have a 2D spatial domain such as

the OAT system, as described in section 2.1. Although, the method easily extends to the 1D case e.g. the flexible beam system. Note that this method does not determine the optimal locations for every available sensor and actuator as this is beyond the scope of this research. Additionally, the location of the actuators is often restricted by physical design choices, making it harder to formulate a general actuator and sensor placement theorem. However, sensor placement for modal identification is highly important. As such, methods to determine optimal sensor locations have been extensively described in [40–46]. Furthermore, when a large number of sensors and actuators are available in a 2D domain such as the wafer stage system, it is generally best to create an equally spaced distribution [23]. Although one should be careful to prevent creating a grid that aligns exactly with the nodal lines of a specific mode shape, as that mode shape will become unobservable.

5.3.1 Mode shape estimation

Knowing the approximate shapes of different modes in a frequency range of interest a priori will allow to determine the optimal collocated sensor placement. To this end, the wafer table of the OAT will be viewed as a rectangle with dimensions 600×600 mm. For such a shape, no closed-form analytical solution exists for determining the mode shapes in an unconstrained situation [47] i.e. where the plate is not connected to the fixed world. There are however many solution approaches that approximate the mode shapes in this case as mentioned in [48, sec. 4.3.15]. The presented solutions often tend to be quite cumbersome though, and thus a more straightforward approach is taken, namely a Finite Element Analysis (FEA). This method also allows to determine the mode shapes for non-uniform 3D objects.

FEA works by discretizing an object into a set of quadratic tetrahedral elements. The physics of each of those elements is then described in the equations of FEA and combined into a larger model that can be solved using partial differential equations. To ensure an accurate result, the element size must be chosen sufficiently small w.r.t. the size of the object that is simulated. An FEA analysis defines how an object will vibrate at certain resonant frequencies, given physical geometry and constraints. Damping effects are ignored and no loads are applied. This means that the absolute out-of-plane displacement amplitude does not have a meaning, only the relative amplitude between positions in the spatial domain. The FEA solver that is used in this research is the Matlab Partial Differential Equation Toolbox whose performance was verified against [49].

In case of a rectangular thin plate, the shape of the modes is most affected by the width and length of the plate. Other parameters such as the thickness and material choice mostly affect the frequencies at which these modes occur. Given the aforementioned plate dimensions and an approximate plate height of 20 mm, an FEA simulation is executed assuming the plate material behaves similarly to aluminum. The first 9 flexible modes are shown in Figure 5.8.

5.3.2 Ideal placement of collocated pairs

The placement of the collocated sensor and actuator pair can be determined by 'overlaying' the relevant flexible modes. In this case, the first 3 simulated modes in Figure 5.8 are used. Since they occur at the lowest frequencies, their contribution is expected to be the largest, and thus accurate identification is most relevant. The absolute amplitude at which each of these modes might oscillate given a certain input disturbance, may vary and is unknown but their nodal lines or Chladni patterns [50] remain the same. The following approach thus provides a method to determine the largest distance from any nodal lines of evaluated modes, which is defined to be an optimal collocated pair location. By normalizing the arbitrary amplitude of each mode shape, they are all weighted equally. Given that the flexible modes are sampled in the domain $\mathfrak{D}(x,y)$, the equation for determining the cost at each (x, y) location, based on the out-of-plane deflection
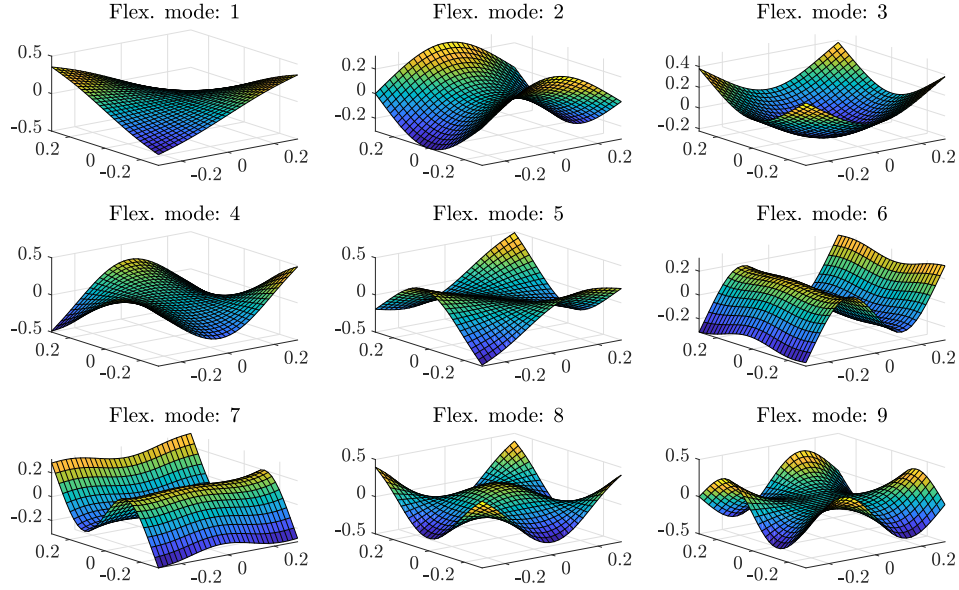
Figure 5.8: The first 9 mode shapes gathered from a finite element analysis of a flat plate, the vertical scaling is arbitrary.
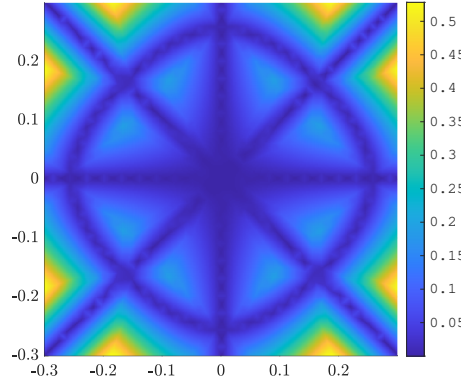

Figure 5.9: Heat map that visualizes proper locations for a collocated sensor and actuator pair as lighter colors.

$z_i(x, y)$ of the selected mode shapes, is

$$\mathcal{Z}(x, y) = \min_{i \in 1,2,3} \left| \frac{z_i(x, y)}{\max_{x,y \in \mathcal{D}} |z_i(x, y)|} \right| \tag{5.10}$$

Due to the discrete nature of the FEA solution method, a global solution that approximates the optimal solution can readily be found by taking the maximum value of $\mathcal{Z}$. Figure 5.9 shows a heat map where the highest values indicate proper sensor locations. Note that there are multiple options due to the symmetric nature of the mode shapes.

5.4   Mode shape interpolation

In this section, two methods will be considered for the interpolation of the spatially sampled mode shapes in $\hat{\mathcal{L}}$ to arrive at a continuous estimate of each mode shape in $\mathcal{L}(\varrho)$. Using simulated test cases, the performance of both methods will be compared to arrive at a recommendation of what to use for modal identification of the OAT system.

5.4.1 Smooth Thin Plate Spline interpolation

The wafer table of the OAT system can be viewed as a thin plate flexible body because its thickness is significantly smaller compared to its width and length. One very common method of approximating the mechanical bending shapes of such thin plates, based on limited spatially distributed samples, is Smooth Thin Plate Spline interpolation (STPS). To this end, consider its cost function given by

$$\min_{\mathcal{W}_s \in \mathfrak{W}_2^1} \sum_{j=1}^{n_\varrho} |\mathcal{W}_s(\bar{x}_j, \bar{y}_j) - \bar{z}_j|^2 + \lambda U, \quad \text{with} \quad U = \int_{-\infty}^{\infty} \int_{-\infty}^{\infty} \Delta^2 \mathcal{W}_s(x, y) dx dy. \tag{5.11}$$

Without going into too much detail, the goal of this optimization is to find an interpolating spline-based function $\mathcal{W}_s$ given n_ϱ points $\{(\bar{x}_j, \bar{y}_j, \bar{z}_j) \in \mathbb{R}^3\}$. This method is generally well-suited since the spline functions are partially determined by minimizing the bending energy U in a thin flexible plate. The other part of this optimization is concerned with reducing the error between a set of spatially distributed known and estimated plate deflections, which constitutes the left term in (5.11). A smoothing parameter λ is used to determine the relative importance of following the available data points and minimizing bending energy. Increasing weight in the latter causes the splines to be smoother and thus more robust against sensor noise. This method and its applications have been extensively discussed in [11, 51, 52] and the formal formulation of this algorithm and its algebraic solution are given in [53]. For completeness, the same algorithm has been provided in appendix A along with the algebraic solution.

In the case of interpolating $\hat{\mathcal{L}}$ to $\mathcal{L}(\varrho)$ for the OAT system, this algorithm must be executed for every mode shape, i.e. every column in $\hat{\mathcal{L}}$. It requires the (x, y) locations along with the corresponding $k = 1, \ldots, n_z$ mode shape samples $[l]_k^i(x_k, y_k)$ found in the columns of $\hat{\mathcal{L}} \in \mathbb{R}^{n_z \times n_m}$, as input. Additionally, the smoothing parameter λ must be provided for each mode shape. In [53, sec. 4] a method for determining this parameter based on the Leave-One-Out Cross Validation (LOOCV) is provided which is further elaborated upon in [23].

The concept of LOOCV is to estimate one of the available points $[l]_m^i(x_m, y_m), m \in 1, \ldots, n_z$ based on information provided by all other available points $[l]_k^i(x_k, y_k), k = \{1, \ldots, n_z | k \neq m\}$. The error between this estimated point $[\hat{l}]_m^i(x_m, y_m, \lambda_i)$ and the known point, that was left out, is stored. By doing this for all points and taking the sum of squared differences, the total LOOCV cost function becomes

$$\mathcal{V}_{cv,i}(\lambda_i) = \sum_{m=1}^{n_z} (\epsilon_{cv,im})^2 \quad with, \quad \epsilon_{cv,im} = [l]_m^i(x_m, y_m) - [\hat{l}]_m^i(x_m, y_m, \lambda_i). \tag{5.12}$$

In case a point m contributes a large value to the cost function, it means that the eventual interpolated surface is significantly affected by that point. Assuming that all sensors function and have similar noise levels, it also indicates that there are fewer sensors near by and thus the estimate at this point could be less robust against sensor noise. To compensate for unequal sensor spacing, an additional weight c_{im} can be added to the cost function, which is now recognized as the generalized cross-covariance cost function [54].

$$\mathcal{V}_{gcv,i}(\lambda_i) = \sum_{m=1}^{n_z} c_{im}(\epsilon_{cv,im})^2. \tag{5.13}$$

The concept of this weighting is to reduce the cost of available points that lie further away from other sensors and to thus rely more on the general surface estimate created by other measurements. The exact mathematical description of the weighting is omitted here for brevity. The optimal value for λ_i can be found by solving the following optimization problem

$$\hat{\lambda}_i = \arg \min_{\lambda_i \in [0, \infty)} \mathcal{V}_{gcv,i}(\lambda_i). \tag{5.14}$$
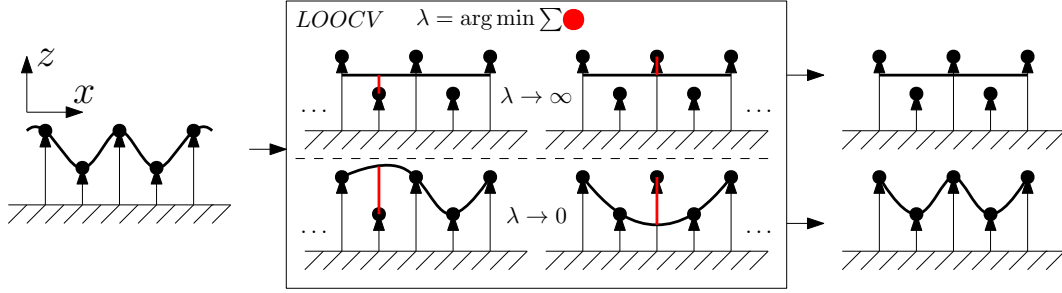
Figure 5.10: Undersensed example of a complex mode shape where LOOCV will incorrectly choose the smoothing parameter to be large.

The optimal solution to this problem can be found using the nonlinear solver `fmincon.m` from the optimization toolbox in MATLAB. Filling the optimal λ into the thin plate spline estimator results is a parametric function that can estimate a mode shape over the entire domain of ϱ.

Potential pitfalls concerning the thin plate spline and smoothing algorithms are mostly related to undersensing. When a limited amount of data is available to identify a complex mode shape, every point is likely to add significantly to the cost function of (5.13) in case of a low smoothing value. LOOCV is therefore more likely to conservatively choose a high smoothing value causing an almost flat surface to be fitted. This is also illustrated in Figure 5.10 for a 1D situation. Analyzing the figure, in case the point density in the x-direction would have been higher, the estimate errors would likely be smaller and thus also a smaller λ would be deemed optimal. In other words, when limited data is available, LOOCV cannot distinguish noise from actual data, because it does not know what the expected noise level is.

Another cause of error might be inadequate sensor and actuator placements. When e.g. all sensors and actuators lie on the nodal lines of a particular mode shape, that shape is not observable and thus a flat plane will once again be fitted. Since no information about any physical properties of the mode shapes is known a priori to the LOOCV algorithm, it will only work well as long as the system is not undersensed for the mode shape to be identified. In [53, sec. 4.9] a similar conclusion is made, it is also mentioned that even with a higher number of data points, it is not guaranteed that the data is fitted as desired.

5.4.2 Interpolation using Gaussian processes

Gaussian processes (GPs) will now be discussed as a potential alternative to thin plate spline interpolation. The latter uses the prior knowledge that the bending energy in a thin plate should always be minimal, but the robustness of the total algorithm is heavily dependent on the number of available data points. It will be shown how GPs can use a different type of prior knowledge of mode shapes to arrive at an estimate that has the potential to perform better than STPS.

GPs can be used to estimate unknown functions using available training data. This is called regression. In case of the OAT, it can be used to estimate a mode shape as a function of (x, y) position on the wafer stage using available plate deflection data from sensors and actuators. A GP is a stochastic process i.e. a set of random variables $f(x)$ indexed by $x \in \mathcal{X}$, with $\mathcal{X} \in \mathbb{R}$ such that any finite subset of them still follows a multivariate Gaussian distribution [55, 56]. It is fully defined by its mean function

$$\mu(x) = \mathbb{E}[f(x)], \tag{5.15}$$

and its covariance function which is also referred to as the kernel function

$$k(x, x') = \mathbb{E}[(f(x) - \mu(x))(f(x') - \mu(x'))] \quad with \quad x, x' \in \mathcal{X}. \tag{5.16}$$

Given this Gaussian distribution, regression on the training data can be performed using Bayesian inference. This process involves updating a probability distribution over functions, called the prior, using observed training data, in order to arrive at a conditioned posterior Gaussian distribution. This distribution now describes an estimate of the underlying function. The type of functions that are fitted are determined by the prior distribution. Since this has the structure of a GP, two functions describing the mean as in (5.15) and the variance as in (5.16) must be defined. The flexible mode shapes of a body are expected to oscillate around a constant plane or axis. There should thus not be any trend present, therefore the mean function is chosen as $\mu(x) = 0$. The covariance function will determine the shape of the functions to be fitted depending on a set of hyper-parameters. A very common choice of covariance function is the squared exponential kernel given by

$$k_{SE}(x, x') = \sigma^2 \exp\left(-\frac{(x - x')^2}{2l^2}\right) \qquad (5.17)$$

In general, this class of functions works well for smooth continuously differentiable functions and can be made to fit a wide variety of them. It is therefore expected to be rich enough to include mode shapes as well. This function has only two hyper-parameters. The first one is the length-scale l. It is a measure for the smoothness of the random function $f(x)$. In case of fitting to a periodic function, this measure should approximately be the length of one period. This hyper-parameter is given for the entire domain to be fitted. Thus, if the local length scale varies a lot, this function class might not yield good results. Extrapolation quality often also worsens significantly beyond approximately l units away from available training data [57]. The second hyper-parameter is the variance σ^2 which determines the average distance between a function and its mean. In (5.17) it is shown that this is basically a scaling factor. For a comprehensive overview of kernels see [56, Sec. 4.2]. Selecting the two hyper-parameters can be done manually based on engineering insight, but they can also be found using marginal likelihood optimization [58]. This algorithm marginalizes the prior over function values based on training data to arrive at optimal hyper-parameters. Note that this is a non-convex optimization problem and thus a decent initial estimate must still be provided manually.

The benefit of this entire framework is that a mean and covariance estimate of the conditioned process can be computed easily. This provides certainty bounds and an expected value of the unknown function that was fitted over the entire relevant domain. Another benefit is that the hyper-parameters allow some information about the function to be explicitly encoded beforehand, which may improve the estimation quality over STPS. Though, this can also be viewed as a downside in comparison to STPS, as the process of finding suitable hyper-parameters is non-trivial. Another potential downside is that the function estimate from GPs is non-parametric. Implementation on a system might thus require lookup tables or a set of polynomials to be fitted.

5.4.3   Finding suitable hyper-parameters

As already mentioned in section 5.4.1, it is likely that the available number of points to identify the mode shapes of the OAT system is limited. Should this set be used to compute the hyper-parameters, the resulting covariance function might not represent the covariance function of the actual mode shape well at all. The fit through the available points may therefore seem decent but might not represent the underlying mode shape properly. By using limited prior knowledge of the OAT system, a modal FEM simulation will now be conducted. The idea is to provide the marginal likelihood optimization algorithm with high-density mode shape information from this simulation. The resulting hyper-parameters can then be used to compute a posterior distribution based on the data points available on the actual setup.

The geometry on which the FEM simulations will be conducted is critical for accurately determining the length scale l in (5.17). This hyper-parameter has the largest influence on the mean

estimate of the posterior distribution. The variance σ^2 is less critical as this value can later be scaled with the ratio between the simulated plate deflection and the measured deflection on the real system. Additionally, this hyper-parameter does not significantly influence the eventual mean estimate of the posterior distribution, it does however heavily influence the variance. The goal of the FEM simulation is thus to gather information about the smoothness of the expected mode shapes.

Since FEM can model any geometry, an obvious choice for the OAT system would be to import the exact geometry of the wafer table which is displayed in Figure 2.4. The figure shows that square and rectangular holes have been created in the bottom of the wafer table in an effort to reduce weight whilst maintaining high stiffness. This will cause the wafer table to bend in a non-homogeneous way. When a marginal likelihood optimization would be executed on a densely sampled version of an arbitrary mode shape of this FEM model, the length scale l will become comparatively small. If this length scale is now used on the OAT system, which has a much smaller data density, the fitting performance will be very poor. In general, relying heavily on a simulated model might also not warrant a robust approach. A better option might be to use a simplified physical model, such as the one used in section 5.3.1. By using this homogeneous plate model, the idea is that only the pure mode shapes are captured, which should contain less information and might thus be better described by the limited hyper-parameter set. This will also create some added robustness against potential sensor noise.

Ideally, the above-mentioned method for identifying hyper-parameters a priori is executed for each mode shape in the FEM model. Yet, here the assumptions are made that 1) all mode shapes of the real system correspond to those in the simulation and 2) they occur in the same order. The latter requirement can be relaxed in case some correlation algorithm could be created that can match available and predicted mode shapes and thus apply suitable hyper-parameters. This is however a questionable approach since there is no guarantee for assumption 1). The best approach might therefore be to select only one set of hyper-parameters to fit all mode shapes and base it on the most complicated shape that is expected.

5.4.4 Performance comparison

In this section, the performance of GP using the accurate and simplified model of the wafer table will be compared against each other and STPS. To this end, the mode shape that is expected to be the most complex, inside the frequency range of interest of the OAT system, is simulated using the accurate and simplified FEM models. The resulting surfaces are colored blue in Figure 5.11. In the figure, the top row shows the fits of GP in red and STPS in green compared to a mode shape derived from the accurate FEM model. The bottom row shows the same type of plots, but now the mode shape reference is derived from the minimal model. Both fitting algorithms are provided with only 13 sample points whose (x, y) position corresponds to the actuator locations on the OAT system, see Figure 2.3 for the exact coordinates. Also consider the 2 leftmost plots in Figure 5.12. Here, the x-axis indicates the number of uniformly distributed points that are provided to the marginal likelihood optimization algorithm, similar to the number of points above each plot in Figure 5.11. The resulting hyper-parameters l and σ are displayed on the y-axis. Subscript $_a$ indicates a parameter based on the accurate FEM model and subscript $_m$ indicates a parameter based on the minimal FEM model of the wafer table. Notice that l_m 'settles' at a larger length scale compared to l_a. l_m also 'settles' quicker compared to l_a, which indicates that more complexity is revealed in the accurate model as the number of sample points increases. Note also that σ_m continues to rise after 200 learning points, whilst σ_a remains somewhat constant. The result of this effect is found in the rightmost plot of Figure 5.12 where clearly, the normalized sum of square errors $e_{GP,m}$ continuous to fall as the magnitude of the fitted function increases, bringing it closer to the reference mode shape. On the contrary, as the number of points used for learning the GP parameters increases, the error $e_{GP,a}$ only worsens and approaches the error of STPS. As a side note, both $e_{STPS,a}$ and $e_{STPS,m}$ do not have a learning step, instead they are
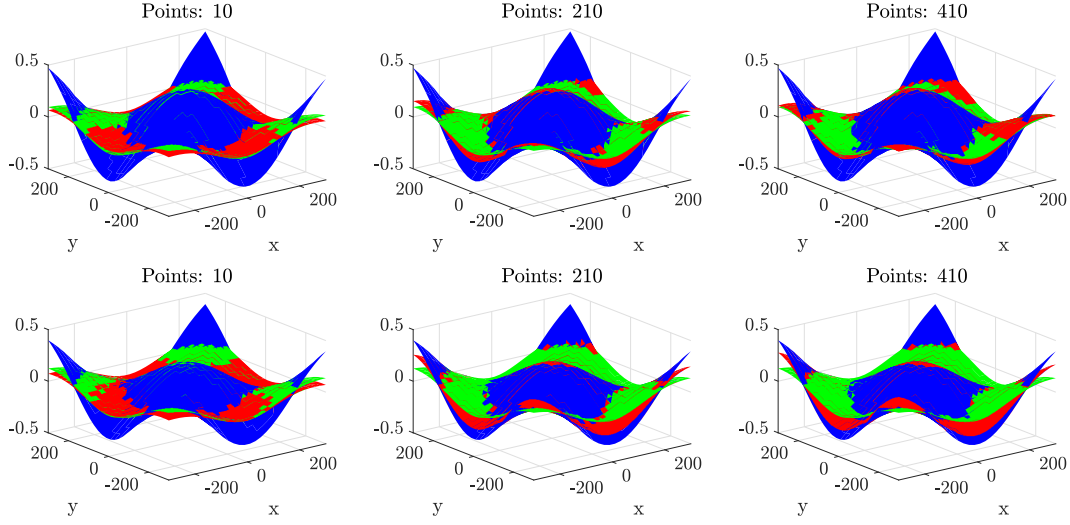
Figure 5.11: Comparison plots showing (–) the reference mode shape from FEM, (–) the fitted surface using STPS and (–) the fitted surface using GPs. Note that both interpolation algorithms use noiseless mode shape information, sampled in the simulation at the actuator locations of the OAT see Figure 2.3. In case of STPS, the hyper-parameters are found based on the number of points mentioned. The top row uses the accurate FEM model and the bottom row uses the minimal FEM model of the wafer table.

directly provided with the 13 sample points of the reference mode shape and are thus constant lines in the figure.

The most important takeaway here is: given a limited set of data points for interpolation, choosing a minimal FEM model to learn the hyper-parameters, rather than a more complex and accurate one, yields a better estimate of the mode shape, also compared to STPS. In general, both algorithms can work. In case a good length scale is found, GP can perform better than spline interpolation. However, finding this value proves to be a non-trivial task. Using FEM simulations, a decent initial guess can be made, which, in those same simulations, leads to a better estimate than STPS, but it is yet to be seen whether this translates to good performance on the real system.
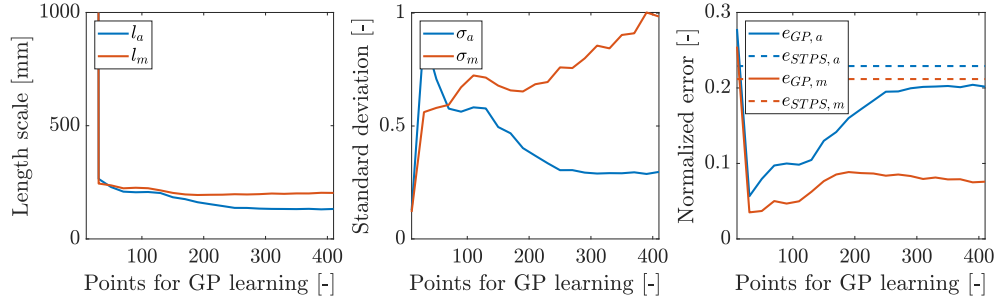
Figure 5.12: Comparison plots that show the hyper-parameters l and σ when using either an **a**ccurate model of the OAT wafer table, indicated by the subscript $_a$ or the **m**inimal model, indicated by $_m$. The rightmost plot compares the normalized sum of squared errors between each interpolation method and the reference mode shape which is shown in Figure 5.11. Note that both methods are only given the points that correspond to the actuator locations of the OAT system as defined in Figure 2.3.

Chapter 6

Experimental results

In this chapter, the methods described to identify an accurate modal model, based on limited non-parametric FRF data, will be experimentally verified. To this end, a distinction is made between validating the performance of the sensor extension method using gain matching as discussed in section 5.2.3 and the performance of interpolation methods as discussed in section 5.4.

6.1 Validation of sensor set extension method

The real flexible beam system, as depicted in Figure 2.6, has three collocated actuator and sensor pairs. This allows the input and output matrices to be compared after the gain matching step has been completed. Ideally, these matrices contain the same information for the collocated pairs, indicating that the method performs well. Similar experiments cannot be conducted on the OAT system as it does not inherently have multiple collocated sensors and actuators. At least two pairs would be necessary, as just having one would always lead to an exact solution for α_i whilst no other comparison can be made without interpolation.

6.1.1 Implementation on the flexible beam system

To test the performance of gain matching on the experimental flexible beam system, a non-parametric identification of the FRF functions of the entire 5×3 system has been conducted as shown in section 4.1.1. Next, a modal model is made that captures the first five mode shapes. The settings used, that correspond to the algorithm as given in section 4.2 are given below.

Modal identification settings. The weighting filter $W(k)$ is chosen to be inverse Schur-weighting with a magnitude cut-off at 40dB. This ensures all frequencies inside the frequency range of interest are weighted equally. Due to the -2 slope in the magnitude plots of the system, frequencies outside this cut-off are automatically weighted less. Additionally, the minima of this weighting were clipped to emphasize accuracy around resonant frequencies. The LMFD is identified with 100 iterations of the SK-algorithm and refined with 10 iterations of the LM-algorithm. The model
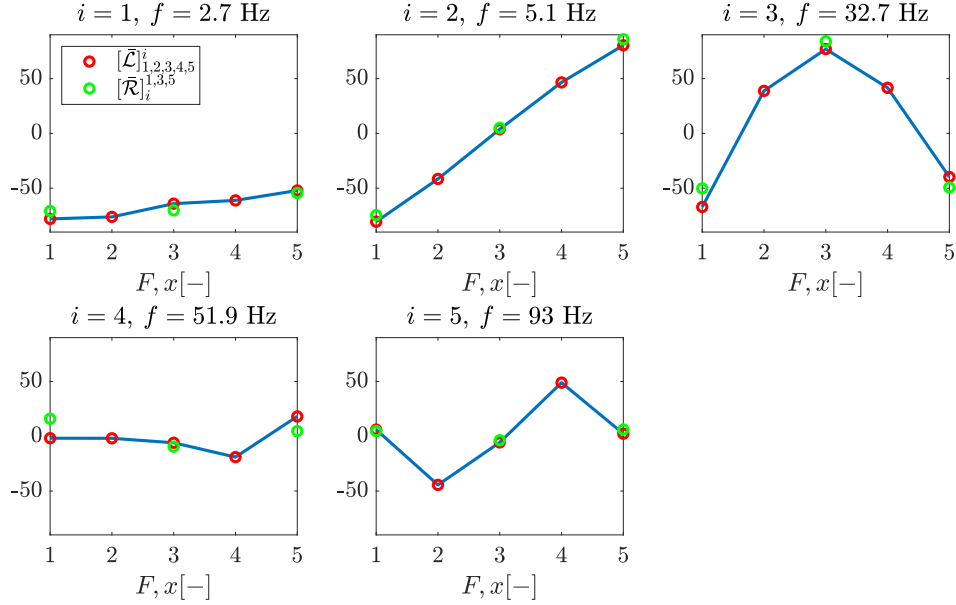
Figure 6.1: The first five mode shapes that have been identified on the real flexible beam system using all available devices, i.e. five sensors and three actuators. A comparison between the rows of the input matrix $\bar{\mathcal{R}}$ and the columns of the output matrix $\bar{\mathcal{L}}$ is shown. Both matrices have been gain matched using the method described in section 5.2.3.

is then transformed to a mechanical model and an additional 10 iterations of the LM-algorithm are performed to improve the fit of this model further.

Lastly, the gain matching procedure is applied based on the three collocated pairs. The resulting columns of the output matrix $\bar{\mathcal{L}}$ and rows of the input matrix $\bar{\mathcal{R}}$, which each correspond to a mode shape, are depicted in Figure 6.1. Here, the x-axes indicate the normalized 1D location of the actuators and sensors on the flexible beam. The first two mode shapes describe the rigid-body behavior of the flexible beam. Note that the beam is suspended by wire flexures and thus these modes do have a non-zero resonance frequency and damping. The stiffness of these flexures also makes the system open-loop stable. Judging from the graphs, the correspondence between the input and output matrices is decent and similar for all modes. Due to mode shape blending effects as described in section 5.2.5, the first two modes should be disregarded for this comparison. Any difference that exists between the data from the input and output matrices may be attributed to non-linear effects or the individual gains of the sensors and actuators. When using the gain matching approach, the assumption is made that all sensors have the same gain i.e., they all measure in equivalent units. The same applies to the actuators, a certain current must induce the same force for every one of them. Another cause of error might be the not globally optimal solution of the modal fitting algorithm. The fourth mode in the figure does not correspond to any of the mode shapes that were found in the simulations, there is also no symmetry, yet it does consistently occur.

The goal of the next experiment is to compare the mode shape identification quality, given all I/O data, against that of hypothetical subsystems where some sensors are left out and replaced by data from the input matrix. To this end, consider Figure 6.2. The legend in the bottom right of the figure indicates what sensor set p was used to produce the mode shape information for modes $i \in 1 \dots 5$. The corresponding resonance frequencies are also mentioned below that in Hertz. The data from all actuators at locations 1, 3, and 5 is available for all experiments. A red circle (o) indicates that a deflection value was taken from the sensor set and a green circle (o) indicates it was taken from the actuator set. The first two rigid-body modes do not contain any information from the actuator set and thus missing points are interpolated. Note that the y-axes are not

scaled equivalently as is the case in Figure 6.1. The blue line in the figure serves as a reference for each mode shape. Clearly, the data of the input matrix $\bar{\mathcal{R}}$ is not equivalent to that in $\bar{\mathcal{L}}$, yet it is highly correlated. Some explanations for this difference have already been provided in the previous paragraph, but another cause could be the choice of the collocated pair. Particularly, in case of the purple experiment where $p \in \{1, 2, 4\}$ and a single collocated pair is available at location 1. For modes 4 and 5 this pair is close to zero and thus gain matching might have limited performance. Ideally, given these mode shapes, location 4 would have a collocated pair as it is never close to zero. Unfortunately, there is no actuator at that location.

The magnitude plots that result from the identified mode shapes, colored blue, yellow, and purple in Figure 6.2, are shown in Figure 6.3. In this magnitude plot, the blue dotted reference fit follows the non-parametric model best across all FRF plots. Comparing this to the yellow and purple models, where one and two sensors have been left out respectively, reveals that the fit quality does decrease. This effect is observed for all rows of FRF plots where a sensor was left out and replaced by actuator information. For example, take the row of x_3 where both the yellow and purple models are missing a sensor. Up until the first flexible mode at 32.7 Hz, the purple model is decent. The yellow model performs better and has a good fit until the second flexible mode at 51.9 Hz.

For the flexible beam system, a full-size model that is created using limited sensor data does perform worse than a model that has all sensors available. Some causes such as sensor or actuator non-linearity, the fitting algorithm, and the choice of collocated pairs have been suggested as possible sources of error. In the next section, the gain matching method is used in combination with interpolation methods to create a modal LPV model of the OAT system. Due to better quality hardware, the proposed method is expected to perform better.
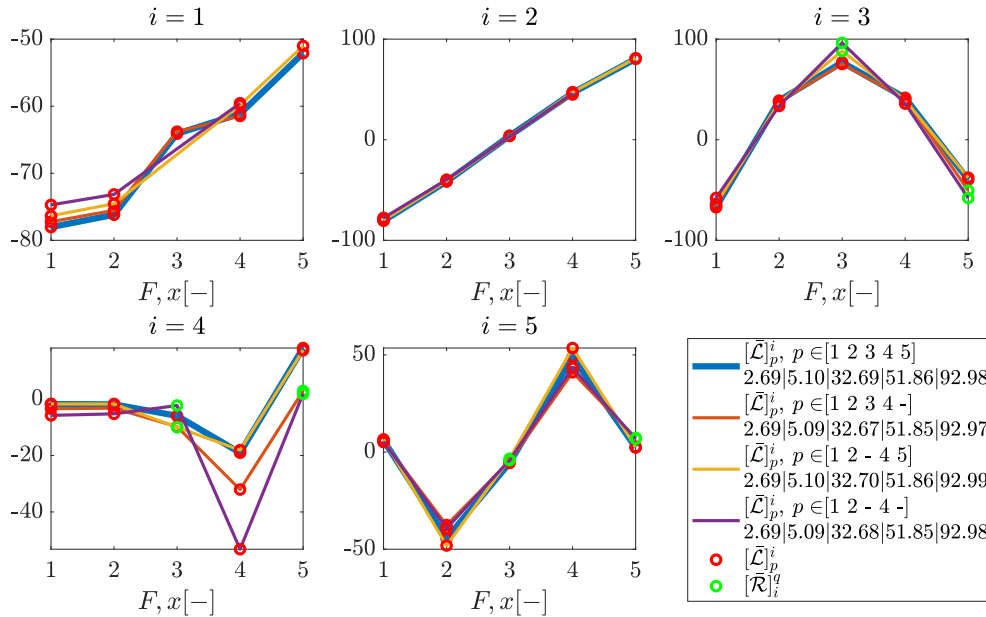

Figure 6.2: Similar to Figure 6.1, but now, a varying number of sensors have been left out as indicated by the set p in the legend. For flexible modes, this missing information is provided by data from the actuator set. The legend also shows the five mode shape resonant frequencies in Hertz for each of the four experiments according to $f_{i=1}|f_{i=2}|\ldots$.

6.2   Validation of interpolation methods

The performance of STPS and GP will now be compared against each other by assessing their overall correlation to the non-parametric FRF data. Given the gain matching approach, interpolation methods are required in case a point of interest has no sensor or actuator close by. During the validation process, this can be simulated by, for example, leaving out data from a non-collocated sensor when creating a modal model. Due to the small number of sensors and actuators on the flexible beam system, leaving out all measurements on one location would significantly worsen the ability of the system to identify mode shapes. Interpolation quality will therefore also be poor after the first or second flexible mode. A better alternative would be to experiment on the OAT system instead, as it has significantly more sensors and actuators which may create a more robust interpolation estimate for a larger number of mode shapes.

6.2.1   Implementation on the OAT

Although the abundance of sensors and actuators makes the OAT a favorable setup for mode shape interpolation, it has no exact collocated sensor and actuator pairs as can be confirmed in Figure 2.3. Each of the four sensors $s_{z_1}, \ldots, s_{z_4}$ does however have an actuator located around 100 mm away, these are $a_{z_1}, \ldots, a_{z_4}$ respectively. In the following experiments, it will be assumed that these sensor and actuator pairs are collocated in order to estimate α_i for the gain matching procedure. During interpolation, the location and measured deflection of the sensor in each collocated pair are used. This ensures that the modal fit is accurate at known sensor locations. Due to mode shape blending, each rigid-body mode is identified using available sensors only. The actuators and sensors in the z-direction of the wafer table control 3-DOF and thus, at least three sensors are required to define each of the rigid-body mode shapes. Since four sensors are available, it will now be attempted to extrapolate data from sensors $s_{z_1}, \ldots, s_{z_3}$ and actuators $a_{z_1}, \ldots, a_{z_{13}}$ to arrive at an estimate of sensor s_{z_4}. Since this data is known, a performance comparison can be conducted
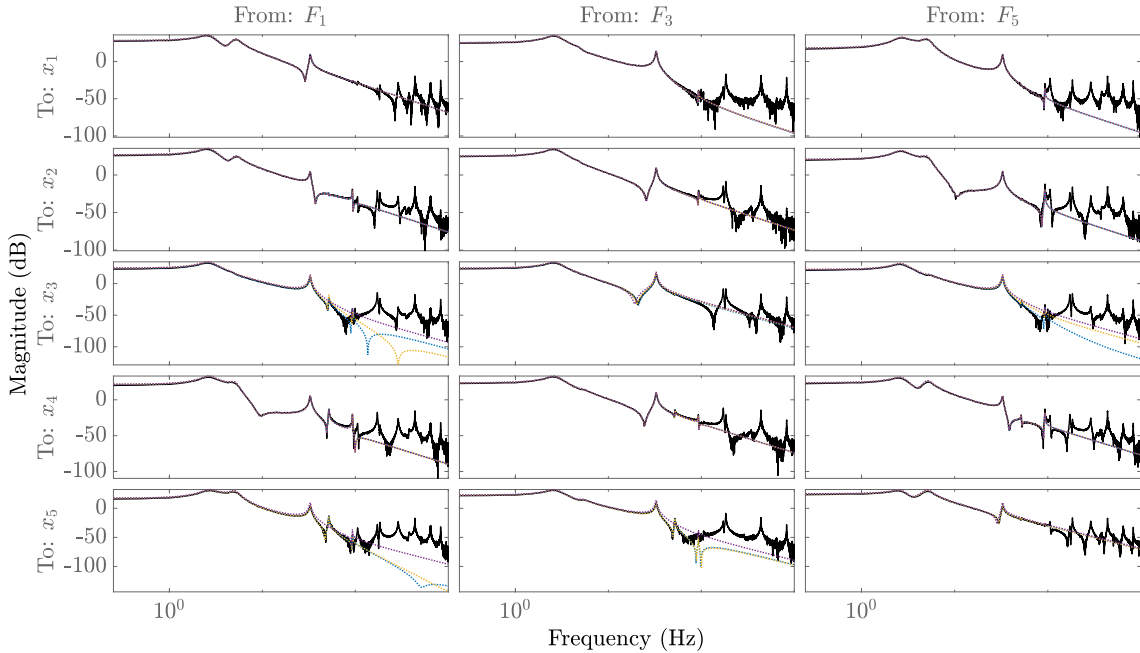

Figure 6.3: 5×3 Magnitude plot of the flexible beam system showing the non-parametric FRF (**–**), the parametric modal model given all available sensors and actuators (**–**), the parametric modal model given all actuators and sensors apart from sensor 3 (**–**), and the modal model given all actuators but only sensors 1, 2 and 4. (**–**).
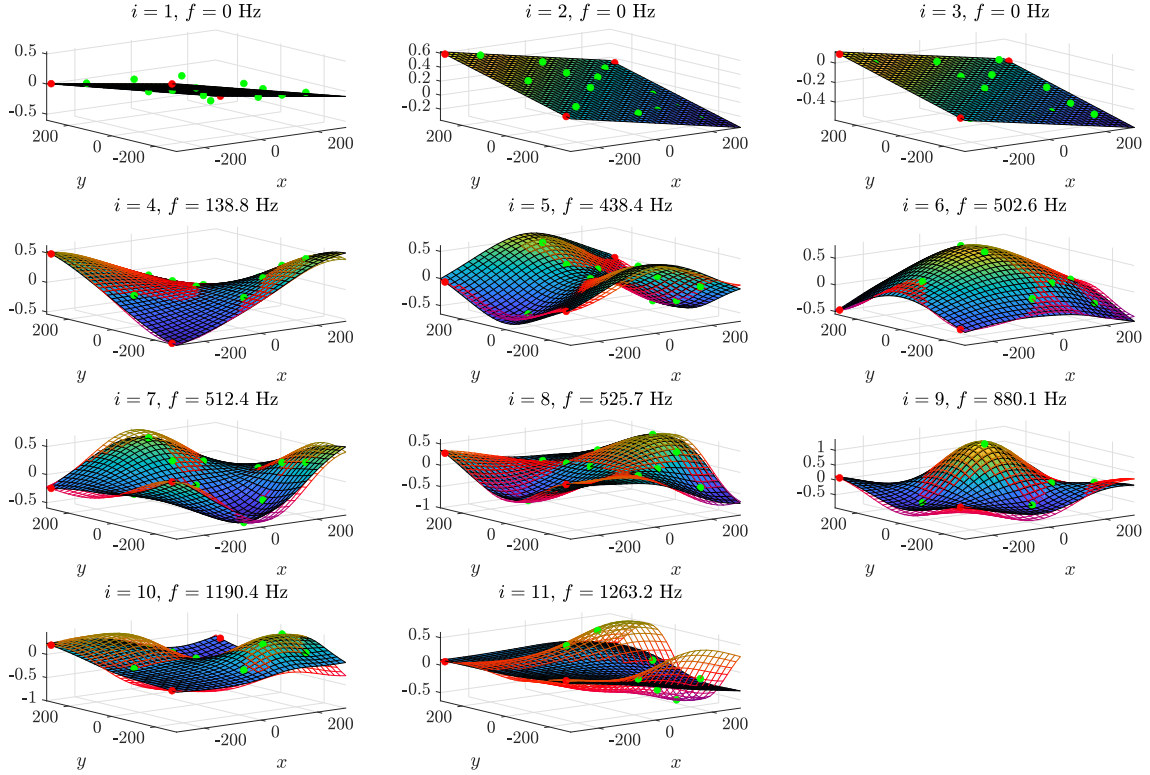
Figure 6.4: Identified mode shapes of the OAT system. Here, the red (•) and green (•) dots in the plots represent gain matched sensor data from $\bar{\mathcal{L}}$ and gain matched actuator data from $\bar{\mathcal{R}}$. The surface plot shows an interpolation made with STPS and the red-toned grid mesh shows an interpolation made with GPs.

for STPS as well as GP interpolation. The parameteric identification settings have once again been listed below.

Modal identification settings. The weighting filter $W(k)$ is chosen to be inverse Schur-weighting with a magnitude cut-off at 80dB. This ensures all frequencies inside the frequency range of interest are weighted equally. Due to the -2 slope in the magnitude plots of the system, frequencies outside this cut-off are automatically weighted less. Additionally, the minima of this weighting were clipped to emphasize accuracy around resonant frequencies. Due to large computation time, the LMFD is identified with only 20 iterations of the SK-algorithm and refined with 10 iterations of the LM-algorithm. The model is then transformed to a mechanical model and an additional 10 iterations of the LM-algorithm are performed to improve the fit of this model further.

Now, consider Figure 6.4, where both STPS and GP interpolated surfaces are displayed per mode shape as blue and red-tinted surfaces, respectively. The red dots, in each of the plots, indicate data taken from the output matrix $\bar{\mathcal{L}}$, and the green dots represent data from the input matrix $\bar{\mathcal{R}}$. Both matrices have been gain matched and can thus be used together to form the surfaces. The mode shapes are recognizable up to the 9th mode, beyond that, both STPS and GP no longer make reliable fits due to undersensing. Note that even though the first three modes were gain matched, the surfaces formed by the actuator set and the sensor set are not the same, as correctly predicted in section 5.2.3.

In general, STPS interpolation creates a more conservative fit compared to GP. The effect that this has on the FRF estimates of sensor s_{z_4} is shown in Figure 6.5. In the figure, the blue (—) colored magnitude represents a modal fit given all sensor data, including s_{z_4}. The orange (—)
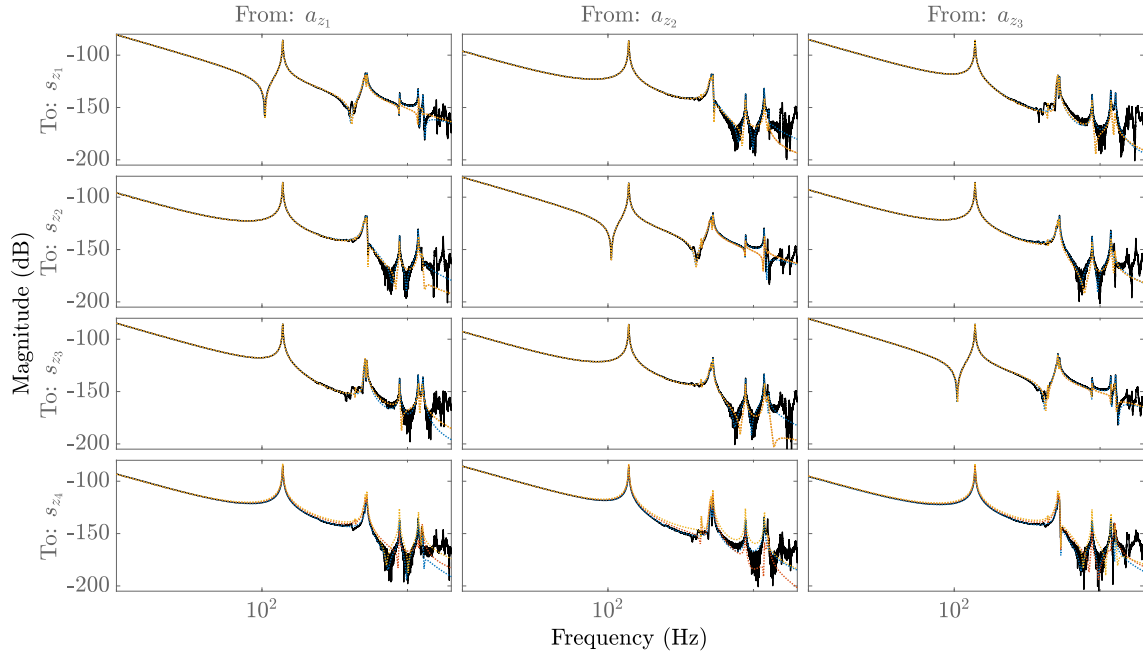
Figure 6.5: Bode diagram showing the magnitude plot from actuator inputs $a_{z_1}, \ldots, a_{z_3}$ to outputs $s_{z_1}, \ldots, s_{z_4}$. Here, (—) is the non-parametric FRF data of the OAT system which serves as a reference, (—) is the modal fit on the FRF data given that all data is available, (—) is a fit made using all actuators but only sensors $s_{z_1}, \ldots, s_{z_3}$. The row of s_{z_4} has been extrapolated using STPS. Similarly, in (—) s_{z_4} has been extrapolated using GPs.

and yellow (—) colored magnitudes are extrapolated using STPS and GP, respectively, whilst s_{z_4} is not available. Compare these to the black (—) colored non-parametric magnitude to determine absolute model quality. The interpolation methods are best compared against the blue fit as it approximates the best possible modal fit given all data. The data displayed in the figure represents a subset of the entire OAT model. Missing columns corresponding to actuators $a_{z_4}, \ldots, a_{z_{13}}$ can be found in appendix B.

Closely observing the row of magnitude plots that correspond to sensor s_{z_4} reveals that the performance of STPS is slightly better compared to GP. It should be noted here that the hyperparameters of the square exponential functions used for GP, are taken directly from simulations of a simplified wafer table model. Knowing that marginal likelihood optimization on a more accurate model indicated a lower length scale, the currently used length scale was lowered somewhat arbitrarily by a third. A single FRF plot from a_{z_1} to s_{z_4} that shows the resulting fit, in green, alongside all previously mentioned fits is shown in Figure 6.6. The reduced length scale improves the interpolation performance and it now surpasses STPS. This shows that GPs have the potential to outperform STPS but with the current approach of estimating the hyper-parameters, this is not yet the case for the OAT system. The overall modal model, created using STPS to interpolate the mode shapes, has decent accuracy until the second flexible mode and can thus help to control the flexible behavior of the wafer table at unmeasured points of interest.
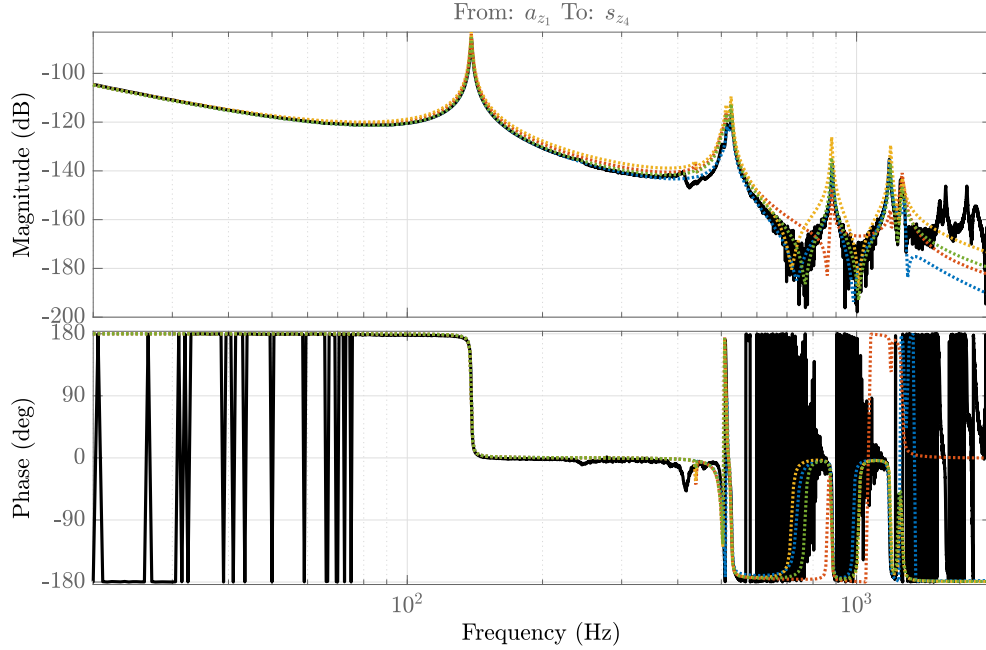
Figure 6.6: Bode diagram showing the magnitude plot from actuator input a_{z_1} to output s_{z_4}. The signals correspond to those in Figure 6.5, except for the green (—) signal which represents a fit using GP where the hyper-parameter l has been reduced by a third.

Chapter 7

Conclusion

The main purpose of this research has been to identify accurate models of the spatio-temporal behavior of systems that consist of a single flexible body and have a limited number of sensors available whilst being overactuated. To this end, a modal modeling approach, that is suitable for systems that have large input/output dimensions and exhibit complex flexible dynamics, is first introduced. Exploiting prior mechanical system knowledge leads to the key insight that the input and output matrices of an identified modal model contain similar information for each mode shape but are sampled at the locations of the actuators and sensors, respectively. Combining information from both matrices is achieved using a collocated pair of sensors and actuators. The concept here is that the actuator and sensor gain of this pair should be equal as their locations are equal. A scaling approach is proposed that enforces this condition.

The location of collocated pairs is determined based on a set of relevant mode shapes that should be identifiable. The concept here is that the scaling approach becomes undefined as soon as the gain of a collocated pair approaches zero. Therefore, a FEM-based approach is proposed that finds areas within the relevant spatial domain where a collocated pair will always measure a sufficiently large gain.

Given that data from actuators and sensors can be combined, a denser grid of points is available to describe the underlying mode shapes. Two interpolation methods are used to reveal these underlying mode shapes given sampled data. The most common method of interpolation, given

that the flexible body of interest can be modeled as a thin plate, is thin plate spline interpolation. Given a low number of samples though, it is found that this method sometimes does not follow the available data points due to the smoothing algorithm used. As an alternative, Gaussian Processes are considered. Here, prior knowledge based on FEM simulations of the same flexible bodies is used to define the smoothness of the expected mode shapes. Both methods show good performance, but based on simulation, Gaussian processes can perform better compared to thin plate spline interpolation.

The effectiveness of the gain matching approach as well as the two interpolation methods have been experimentally verified on two systems. The performance of gain matching is decent but the location of the collocated pair must be such that it is not on a nodal point or line of a relevant mode. This approach also requires actuators to respond linearly and their gains to be equivalent or exactly known, which may not always be the case. The proposed method of interpolation using Gaussian Processes is shown to have the potential to outperform Smooth Thin Plate Spline interpolation. The current method of finding a suitable length scale using FEM simulations is however not able to produce optimal values yet, and thus STPS still performs slightly better.

This thesis provides a unified approach for the identification of the spatio-temporal system behavior of next-generation motion systems. Prior mechanical system knowledge is used to more accurately estimate the flexible behavior spatially, than previously possible. The effectiveness of the proposed approach is demonstrated on two benchmark experimental systems.

Recommendations and future research

In case the approaches mentioned in this thesis are applied to overactuated mechanical systems, the following advice is provided. The gain of the actuators should either be known or measurable. Given that the sensors also have a consistent gain, this will ensure the best performance for the gain matching procedure. In case there is design freedom in actuator and sensor placement in a particular system, a FEM simulation can be used to determine the optimal locations of the collocated sensor pairs by observing the mode shapes in the relevant frequency range of interest. These should be placed such that the situation in which all of them measure a low gain for a particular mode shape is avoided to ensure accuracy. The best and most robust interpolation approach is currently the thin plate spline method. However, in case a system has, for example, one more sensor than the number of degrees of freedom, that additional sensor can be used for validation. In that case, the approach that uses Gaussian Processes can be used. An initial estimate of the hyper-parameters can be found using the given approach, which can then be optimized by minimizing error between the interpolation estimate and the real value as measured by the validation sensor.

Future research may concern a method to more accurately find the optimal hyper-parameters for estimation using Gaussian Processes. The framework of Gaussian Processes provides significant design freedom which can also be explored more. The kernel that defines the covariance function can, for example, be tailored more specifically to each mode shape. This way, properties such as symmetry can be incorporated more effectively.

Currently, the GP framework is only used to estimate the mean of the mode shapes, but it also produces a variance. Potentially, this can be used in combination with uncertainty estimation of the non-parametric and parametric identification methods to arrive at an estimate of the total model uncertainty. Confidence intervals for Thin Plate Spline interpolation have also been discussed in [53]. It may be possible to estimate the total model uncertainty using this method as well.

The main purpose of this thesis has been to identify accurate models of the spatio-temporal system behavior. After such a model is obtained, the next step would be to use it for synthesizing a controller using a model-based approach such as inferential or observer-based control. Implementing this on a system will allow the performance to be compared to more traditional control approaches.

Appendix A

Spline interpolation algorithm

In this section, the smooth-thin-plate-spline (STPS) interpolation algorithm from [11] is provided. The goal of this algorithm is to find an interpolating function $\mathcal{W}_s \in \mathfrak{W}_2^1$ given a smoothing parameter $\lambda \in [0, \infty]$ and a set of n_ϱ points $\{(\bar{x}_j, \bar{y}_j, \bar{z}_j) \in \mathbb{R}^3\}$ which are spatially distributed in (x, y) directions. Here, $\mathfrak{W}_2^1$ defines the set of functions that is continuously differentiable with square-integrable second derivatives. The cost function to find an optimal $\mathcal{W}_s$ is given by,

$$\min_{\mathcal{W}_s \in \mathfrak{W}_2^1} \sum_{j=1}^{n_\varrho} |\mathcal{W}_s(\bar{x}_j, \bar{y}_j) - \bar{z}_j|^2 + \lambda U, \tag{A.1}$$

with

$$U = \int_{-\infty}^{\infty} \int_{-\infty}^{\infty} \Delta^2 \mathcal{W}_s(x, y) dx dy. \tag{A.2}$$

The functions that minimize (A.1) are given by

$$\mathcal{W}_s(x, y, \vartheta) = \vartheta_0 + x\vartheta_x + y\vartheta_y + \sum_{j=1}^{n_\varrho} \vartheta_j G_j(x, y), \tag{A.3}$$

$$G_j(x, y) = r_j^2 \ln(r_j), \quad r_j = \sqrt{(\bar{x}_j - x)^2 + (\bar{y}_j - y)^2}, \tag{A.4}$$

where $G_j(x, y)$ are so-called green's functions [59]. The first 3 terms on the right-hand side of (A.3) represent a set of first-order polynomials that lie in the null space of U. The following three additional constraints are necessary to ensure this function space remains orthogonal to that of $G_j(x, y)$.

$$\sum_{j=1}^{n_\varrho} \vartheta_j = 0, \quad \sum_{j=1}^{n_\varrho} \vartheta_j \bar{x}_j = 0, \quad \sum_{j=1}^{n_\varrho} \vartheta_j \bar{y}_j = 0. \tag{A.5}$$

Given these constraints and the function space defined by $\mathcal{W}_s$, the solution to (A.1) in matrix form is given by

$$\vartheta = X^{-1} \begin{bmatrix} \bar{z}_1 & \dots & \bar{z}_{n_\varrho} & \mathbf{0}_{1 \times 3} \end{bmatrix}^\top, \quad \vartheta = \begin{bmatrix} \vartheta_0 & \vartheta_x & \vartheta_y & \vartheta_1 & \dots & \vartheta_{n_\varrho} \end{bmatrix}^\top, \tag{A.6}$$

with

$$X = \begin{bmatrix} X_0 & X_G + \lambda I \\ \mathbf{0}_{3 \times 3} & X_0^\top \end{bmatrix}, \quad X_0 = \begin{bmatrix} 1 & \bar{x}_1 & \bar{y}_1 \\ & \vdots & \\ 1 & \bar{x}_{n_\varrho} & \bar{y}_{n_\varrho} \end{bmatrix},$$

$$X_G = \begin{bmatrix} G_1(\bar{x}_1, \bar{y}_1) & \dots & G_{n_\varrho}(\bar{x}_1, \bar{y}_1) \\ \vdots & & \vdots \\ G_1(\bar{x}_{n_\varrho}, \bar{y}_{n_\varrho}) & \dots & G_{n_\varrho}(\bar{x}_{n_\varrho}, \bar{y}_{n_\varrho}) \end{bmatrix}. \tag{A.7}$$
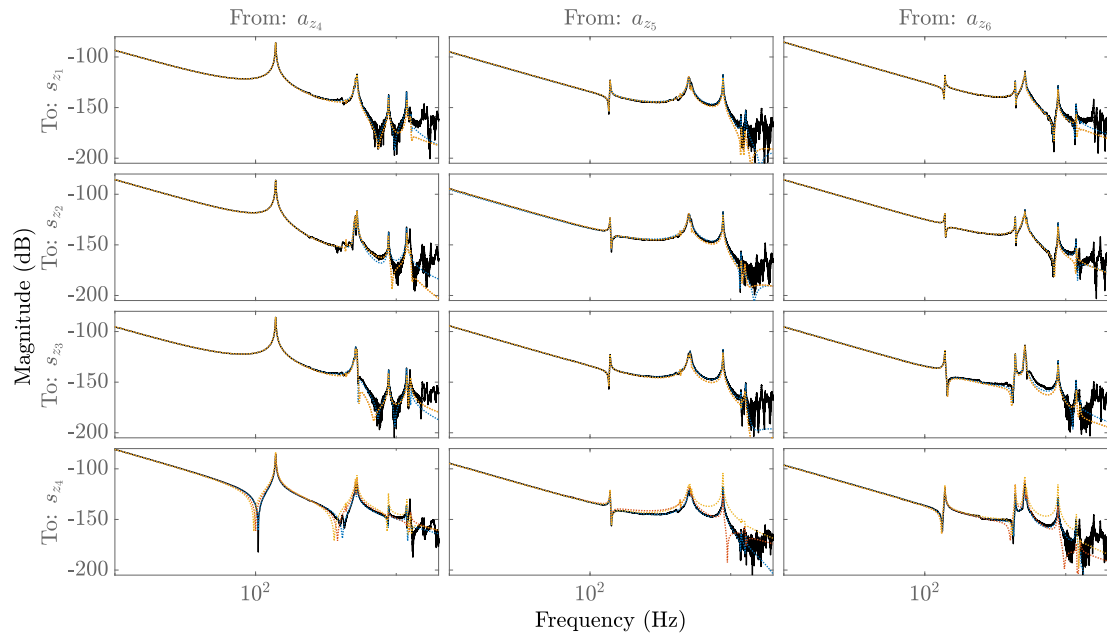
Appendix B

Modal fits of OAT system

Figure B.1: Bode diagram showing the magnitude plot from actuator inputs $a_{z_4}, \ldots, a_{z_6}$ to outputs $s_{z_1}, \ldots, s_{z_4}$. Here, (—) is the non-parametric FRF data of the OAT system which serves as a reference, (—) is the modal fit on the FRF data given that all data is available, (—) is a fit made using all actuators but only sensors $s_{z_1}, \ldots, s_{z_3}$. The row of s_{z_4} has been extrapolated using STPS. Similarly, in (—) s_{z_4} has been extrapolated using GPs.
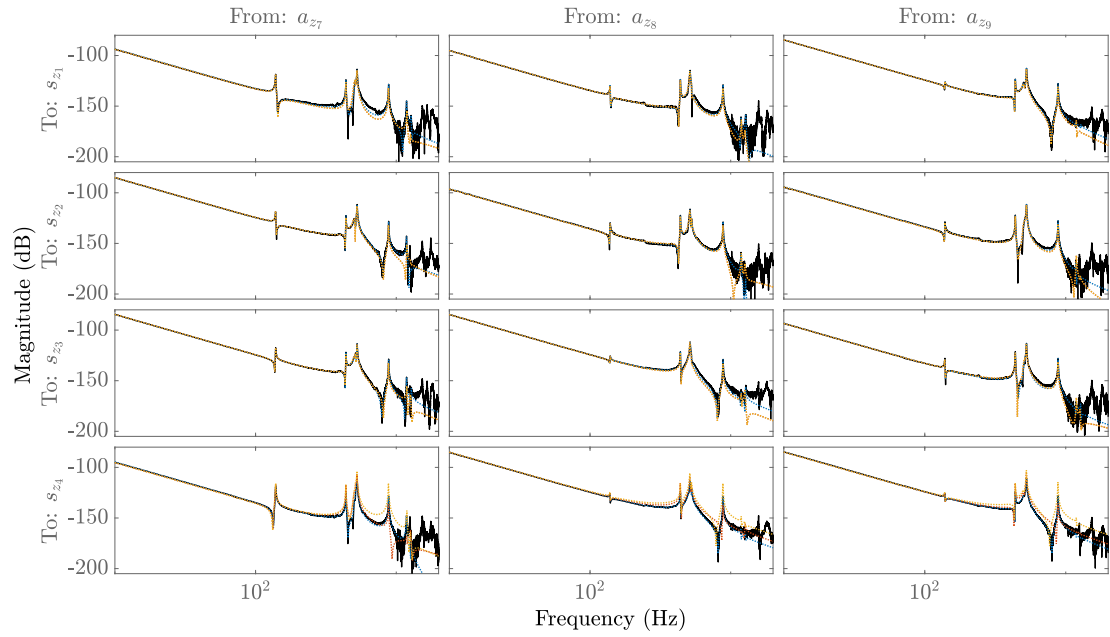
Figure B.2: Bode diagram showing the magnitude plot from actuator inputs $a_{z_7}, \ldots, a_{z_9}$ to outputs $s_{z_1}, \ldots, s_{z_4}$. Here, the plot colors correspond to those of Figure B.1.
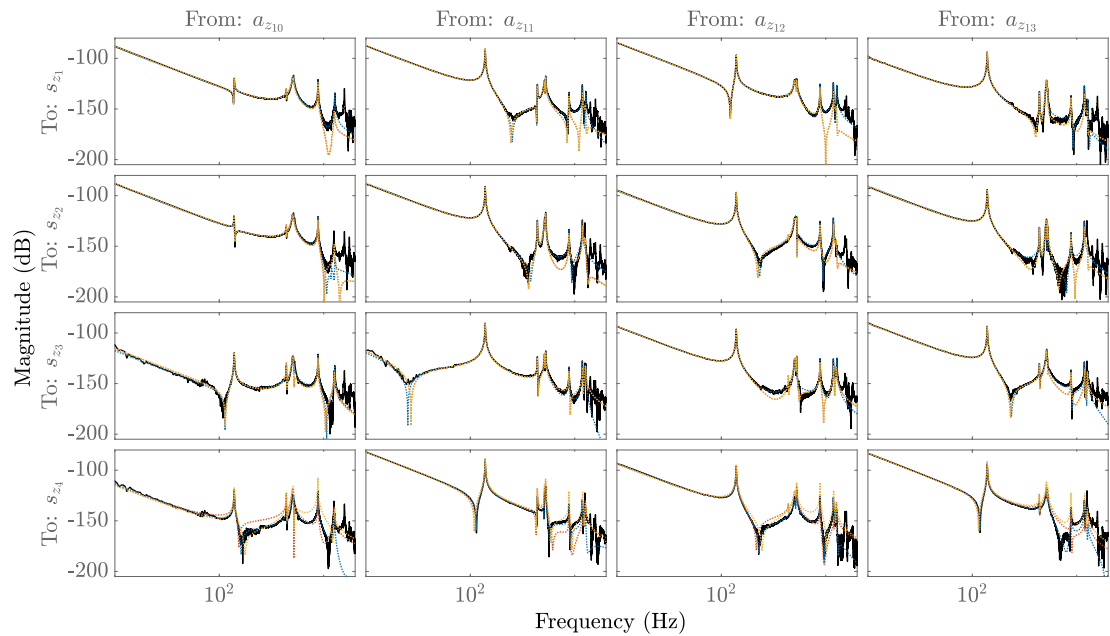

Figure B.3: Bode diagram showing the magnitude plot from actuator inputs $a_{z_{10}}, \ldots, a_{z_{13}}$ to outputs $s_{z_1}, \ldots, s_{z_4}$. Here, the plot colors correspond to those of Figure B.1.

Appendix C

Rigid-body freedom example

In this section, the domain containing all possible input and output vectors to construct a particular rigid body matrix is shown. It is assumed here that the rigid body matrix is square positive definite and symmetric due to the vectors that it is constructed from

$$R_{rb} \in \mathbb{R}^{2 \times 2}, R_{rb} > 0 \Leftrightarrow R_{rb} = \phi_1 \phi_1^\top + \phi_2 \phi_2^\top. \tag{C.1}$$

The matrix R_{rb} can be arbitrarily separated into a sum of vector products using a singular value decomposition

$$R_{rb} = U \Sigma V^\top = U \Sigma U^\top = \tilde{U} \tilde{U}^\top = \tilde{u}_1 \tilde{u}_1^\top + \tilde{u}_2 \tilde{u}_2^\top. \tag{C.2}$$

From these vectors, a new set of vectors can be created namely

$$\hat{u}_1 = \alpha_1 \tilde{u}_1 + \alpha_2 \tilde{u}_2$$
$$\hat{u}_2 = \beta_1 \tilde{u}_1 + \beta_2 \tilde{u}_2. \tag{C.3}$$

Such that

$$\hat{R}_{rb} = \hat{u}_1 \hat{u}_1^\top + \hat{u}_2 \hat{u}_2^\top,$$
$$\hat{R}_{rb} = \left(\alpha_1^2 + \beta_1^2 \right) \tilde{u}_1 \tilde{u}_1^\top + (\alpha_1 \alpha_2 + \beta_1 \beta_2) \left(\tilde{u}_1 \tilde{u}_2^\top + \tilde{u}_2 \tilde{u}_1^\top \right) + \left(\alpha_2^2 + \beta_2^2 \right) \tilde{u}_2 \tilde{u}_2^\top. \tag{C.4}$$

Since the newly found matrix $\hat{R}_{rb}$ must be equal to the original matrix R_{rb}, the following conditions hold

$$\hat{R}_{rb} = R_{rb} \Rightarrow \begin{cases} \alpha_1^2 + \beta_1^2 = 1 \\ \alpha_1 \alpha_2 + \beta_1 \beta_2 = 0 \\ \alpha_2^2 + \beta_2^2 = 1 \end{cases} \tag{C.5}$$

There are now four variables and three equations, meaning one of them can be chosen freely in $[0, 1]$. When α_1 is defined to be the free variable, solving the constraints yields four possible solutions for every value of α_1. These solutions have been provided in Table C.1. The possible vectors $\hat{u}_1$ and $\hat{u}_2$ are also displayed over their entire domain in Figure C.1. Here, the red lines depict the two scalars in $\hat{u}_1(\alpha_1)$ and blue depicts $\hat{u}_2(\alpha_1)$. The vectors that form R_{rb} were chosen arbitrarily to be $\phi_1 = \begin{bmatrix} 1 & 2 \end{bmatrix}^\top$ and $\phi_2 = \begin{bmatrix} -1 & 4 \end{bmatrix}^\top$. The figure shows that given a rigid body matrix of size 2×2, it is possible to find a decoupling for which one mode has a true translation.

$\alpha_2 = -\frac{\beta_1 \beta_2}{\alpha_1}$	$\beta_1 = \sqrt{1 - \alpha_1^2}$	$\beta_1 = -\sqrt{1 - \alpha_1^2}$
$\beta_2 = \alpha_1$	$\hat{u}_1 = \alpha_1 \tilde{u}_1 - \sqrt{1 - \alpha_1^2} \tilde{u}_2$ $\hat{u}_2 = \sqrt{1 - \alpha_1^2} \tilde{u}_1 + \alpha_1 \tilde{u}_2$	$\hat{u}_1 = \alpha_1 \tilde{u}_1 + \sqrt{1 - \alpha_1^2} \tilde{u}_2$ $\hat{u}_2 = -\sqrt{1 - \alpha_1^2} \tilde{u}_1 + \alpha_1 \tilde{u}_2$
$\beta_2 = -\alpha_1$	$\hat{u}_1 = \alpha_1 \tilde{u}_1 + \sqrt{1 - \alpha_1^2} \tilde{u}_2$ $\hat{u}_2 = \sqrt{1 - \alpha_1^2} \tilde{u}_1 - \alpha_1 \tilde{u}_2$	$\hat{u}_1 = \alpha_1 \tilde{u}_1 - \sqrt{1 - \alpha_1^2} \tilde{u}_2$ $\hat{u}_2 = -\sqrt{1 - \alpha_1^2} \tilde{u}_1 - \alpha_1 \tilde{u}_2$

Table C.1: Displays all possible vector combinations for which it holds that $\hat{R}_{rb} = R_{rb}$ with $\alpha_1 \in [0, 1]$.
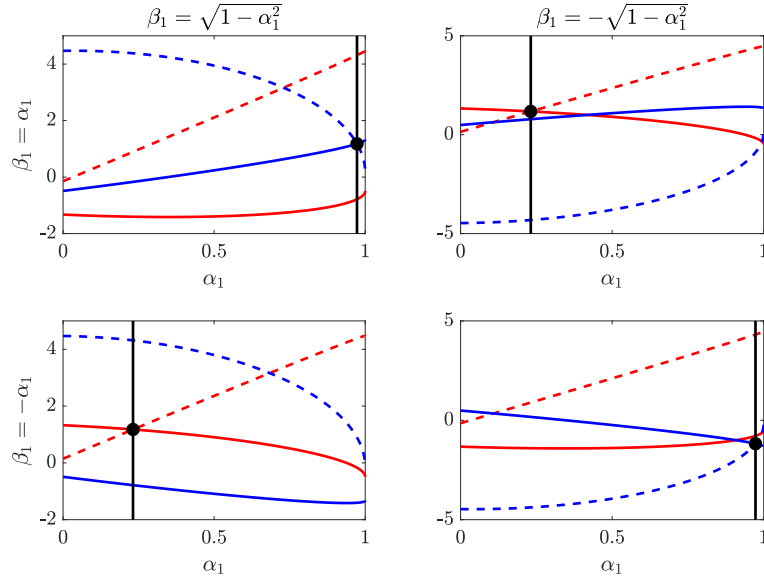
Figure C.1: Displays the four possible solutions for vectors $\hat{u}_1$ and $\hat{u}_2$ given the domain of α_1. The red lines indicate the scalars in $\hat{u}_1$ and the blue lines indicate the scalars in $\hat{u}_2$. The vertical black lines indicate a value of α_1 for which either $\hat{u}_1$ or $\hat{u}_2$ contains equivalent values.

Bibliography

[1] J. W. Hardy, *Adaptive optics for astronomical telescopes*. Oxford University Press on Demand, 1998, vol. 16. 1

[2] G. Witvoet, J. Nijenhuis, and L. Kramer, "Dynamic testing of primary mirror segment supports for the extremely large telescope," in *Ground-based and Airborne Telescopes VII*, vol. 10700. International Society for Optics and Photonics, 2018, p. 107003J. 1

[3] T. Oomen, R. van Herpen, S. Quist, M. van de Wal, O. Bosgra, and M. Steinbuch, "Next-generation wafer stage motion control: Connecting system identification and robust control," in *2012 American Control Conference (ACC)*. IEEE, 2012, pp. 2455–2460. 1

[4] J. Bolder and T. Oomen, "Inferential iterative learning control: A 2d-system approach," *Automatica*, vol. 71, pp. 247–253, 2016. 1

[5] T. Oomen, E. Grassens, and F. Hendriks, "Inferential motion control: Identification and robust control framework for positioning an unmeasurable point of interest," *IEEE Transactions on control systems technology*, vol. 23, no. 4, pp. 1602–1610, 2014. 1

[6] M. Van de Wal, G. van Baars, F. Sperling, and O. Bosgra, "Multivariable $\mathcal{H}_\infty/\mu$ feedback control design for high-precision wafer stage motion," *Control engineering practice*, vol. 10, no. 7, pp. 739–755, 2002. 1

[7] J. Bolder, T. Oomen, and M. Steinbuch, "On inferential iterative learning control: with example to a printing system," in *2014 American Control Conference*. IEEE, 2014, pp. 1827–1832. 1

[8] J. van Zundert and T. Oomen, "On optimal feedforward and ilc: The role of feedback for optimal performance and inferential control," *IFAC-PapersOnLine*, vol. 50, no. 1, pp. 6093–6098, 2017. 1

[9] T. Oomen, R. van Herpen, S. Quist, M. van de Wal, O. Bosgra, and M. Steinbuch, "Connecting system identification and robust control for next-generation motion control of a wafer stage," *IEEE Transactions on Control Systems Technology*, vol. 22, no. 1, pp. 102–118, 2013. 1

[10] R. Voorhoeve, R. de Rozario, and T. Oomen, "Identification for motion control: Incorporating constraints and numerical considerations," in *2016 American Control Conference (ACC)*. IEEE, 2016, pp. 6209–6214. 1

[11] R. Voorhoeve, R. D. Rozario, W. Aangenent, and T. Oomen, "Identifying position-dependent mechanical systems: A modal approach applied to a flexible wafer stage," *IEEE Transactions on Control Systems Technology*, vol. 29, pp. 194–206, 1 2021. 1, 2, 13, 14, 17, 26, 40

[12] W. K. Gawronski, *Dynamics and control of structures: A modal approach.* Springer Science & Business Media, 2004. 1

[13] C. Hoffmann and H. Werner, "A survey of linear parameter-varying control applications validated by experiments or high-fidelity simulations," *IEEE Transactions on Control Systems Technology*, vol. 23, no. 2, pp. 416–433, 2014. 1

[14] J. Mohammadpour and C. W. Scherer, *Control of linear parameter varying systems with applications.* Springer Science & Business Media, 2012. 1

[15] C. W. Scherer, "Lpv control and full block multipliers," *Automatica*, vol. 37, no. 3, pp. 361–375, 2001. 1

[16] C. A. Herrera, D. M. McFarland, L. A. Bergman, and A. F. Vakakis, "Methodology for nonlinear quantification of a flexible beam with a local, strong nonlinearity," *Journal of Sound and Vibration*, vol. 388, pp. 298–314, 2017. 2

[17] A. Ghali, A. M. Neville, and T. G. Brown, *Structural Analysis: A unified classical and matrix approach 6th edition.* Crc Press, 2017. 2

[18] MI-Partners, *User Manual: Over Actuated Test rig*, 2010. 6

[19] H. Soemers, *Design principles for precision mechanisms.* Netherlands: University of Twente, 2010. 7

[20] H.-X. Li and C. Qi, "Modeling of distributed parameter systems for applications—a synthesized review from time–space separation," *Journal of Process Control*, vol. 20, no. 8, pp. 891–901, 2010. 9

[21] D. J. Ewins, *Modal testing: theory, practice and application.* John Wiley & Sons, 2009. 10

[22] B. de Kraker, "A numerical-experimental approach in structural dynamics, 2000," *Lecture notes*, no. 4748, 2004. 10

[23] R. de Rozario, R. Voorhoeve, W. Aangenent, and T. Oomen, "Identifying position-dependent mechanical systems: a physics-based lpv approach, with application to a wafer stage," in *25th European Research Network System Identification (ERNSI) Workshop, 25-28 September 2016, Cison di Valmarino, Italy*, 2016. 10, 24, 26

[24] T. Oomen, R. V. Herpen, S. Quist, M. van de Wal, O. Bosgra, and M. Steinbuch, "Connecting system identification and robust control for next-generation motion control of a wafer stage," *IEEE Transactions on Control Systems Technology*, vol. 22, 2014. 12

[25] R. Pintelon and J. Schoukens, *System identification: a frequency domain approach.* John Wiley & Sons, 2012. 12

[26] J. Schoukens, A. Marconato, R. Pintelon, Y. Rolain, M. Schoukens, K. Tiels, L. Vanbeylen, G. Vandersteen, and A. Van Mulders, "System identification in a real world," in *2014 IEEE 13th International Workshop on Advanced Motion Control (AMC)*. IEEE, 2014, pp. 1–9. 12

[27] J. Schoukens, R. Pintelon, and Y. Rolain, *Mastering system identification in 100 exercises*. John Wiley & Sons, 2012. 12

[28] P. E. Wellstead, "Non-parametric methods of system identification," *Automatica*, vol. 17, no. 1, pp. 55–69, 1981. 13, 14

[29] K. Classens, M. Mostard, J. van de Wijdeven, W. M. Heemels, and T. Oomen, "Fault detection for precision mechatronics: Online estimation of mechanical resonances," *IFAC-PapersOnLine*, vol. 55, no. 37, pp. 746–751, 2022. 13

[30] E. Evers, R. Voorhoeve, and T. Oomen, "On frequency response function identification for advanced motion control," in *2020 IEEE 16th International Workshop on Advanced Motion Control (AMC)*. IEEE, 2020, pp. 1–6. 14

[31] M. Mostard, "Fault diagnosis to controller reconfiguration: With application to high-precision mechatronics," Master's thesis, Eindhoven University of Technology, jan 2023. 14

[32] K. Glover and J. Willems, "Parametrizations of linear dynamical systems: Canonical forms and identifiability," *IEEE Transactions on Automatic Control*, vol. 19, no. 6, pp. 640–646, 1974. 15

[33] C. Sanathanan and J. Koerner, "Transfer function synthesis as a ratio of two complex polynomials," *IEEE transactions on automatic control*, vol. 8, no. 1, pp. 56–58, 1963. 15

[34] J. J. Moré, "The levenberg-marquardt algorithm: implementation and theory," in *Numerical analysis*. Springer, 1978, pp. 105–116. 15

[35] C.-Y. Wang, C.-H. Chiang, and C.-K. Huang, "Damage assessment of structure by the reciprocal theorem of elastodynamics and the frequency domain decomposition (fdd) method," 2005. 16

[36] Z. Sun, T. Nagayama, and Y. Fujino, "Minimizing noise effect in curvature-based damage detection," *Journal of Civil Structural Health Monitoring*, vol. 6, no. 2, pp. 255–264, 2016. 16

[37] I.-Y. Choi, J. S. Lee, E. Choi, and H.-N. Cho, "Development of elastic damage load theorem for damage detection in a statically determinate beam," *Computers & Structures*, vol. 82, no. 29-30, pp. 2483–2492, 2004. 16

[38] R. Voorhoeve, A. van der Maas, and T. Oomen, "Non-parametric identification of multivariable systems: A local rational modeling approach with application to a vibration isolation benchmark," *Mechanical Systems and Signal Processing*, vol. 105, pp. 129–152, 2018. 17

[39] L. Meirovitch and R. Parker, "Fundamentals of vibrations," *Appl. Mech. Rev.*, vol. 54, no. 6, pp. B100–B101, 2001. 17

[40] C. Stephan, "Sensor placement for modal identification," *Mechanical Systems and Signal Processing*, vol. 27, pp. 461–470, 2012. 24

[41] D. C. Kammer, "Optimal sensor placement for modal identification using system-realization methods," *Journal of Guidance, Control, and Dynamics*, vol. 19, no. 3, pp. 729–731, 1996. 24

[42] L. He, J. Lian, B. Ma, and H. Wang, "Optimal multiaxial sensor placement for modal identification of large structures," *Structural Control and Health Monitoring*, vol. 21, no. 1, pp. 61–79, 2014. 24

[43] K. Lim, "Method for optimal actuator and sensor placement for large flexible structures," *Journal of Guidance, Control, and Dynamics*, vol. 15, no. 1, pp. 49–57, 1992. 24

[44] W. Gawronski and K. Lim, "Balanced actuator and sensor placement for flexible structures," *International Journal of Control*, vol. 65, no. 1, pp. 131–145, 1996. 24

[45] W. Liu, Z. Hou, and M. A. Demetriou, "A computational scheme for the optimal sensor/actuator placement of flexible structures using spatial h2 measures," *Mechanical systems and signal processing*, vol. 20, no. 4, pp. 881–895, 2006. 24

[46] C. Westermayer, A. Schirrer, M. Hemedi, and M. Kozek, "An advanced criterion for optimal actuator and sensor placement on complex flexible structures," *IFAC Proceedings Volumes*, vol. 42, no. 2, pp. 114–119, 2009. 24

[47] S. Hurlebaus, L. Gaul, and J.-S. Wang, "An exact series solution for calculating the eigenfrequencies of orthotropic plates with completely free boundary," *Journal of Sound and Vibration*, vol. 244, no. 5, pp. 747–759, 2001. 24

[48] A. W. Leissa, *Vibration of plates.* Scientific and Technical Information Division, National Aeronautics and . . . , 1969, vol. 160. 24

[49] N. A. for Finite Element Methods & Standards, *The Standard NAFEMS Benchmarks.* National Agency for Finite Element Methods & Standards, 1990. 24

[50] P. Tuan, C. Wen, P. Chiang, Y. Yu, H.-C. Liang, K.-F. Huang, and Y.-F. Chen, "Exploring the resonant vibration of thin plates: Reconstruction of chladni patterns and determination of resonant wave numbers," *The Journal of the Acoustical Society of America*, vol. 137, no. 4, pp. 2113–2123, 2015. 24

[51] W. Keller and A. Borkowski, "Thin plate spline interpolation," *Journal of Geodesy*, vol. 93, no. 9, pp. 1251–1269, 2019. 26

[52] A. Borkowski and W. Keller, "Global and local methods for tracking the intersection curve between two surfaces," *Journal of Geodesy*, vol. 79, no. 1, pp. 1–10, 2005. 26

[53] G. Wahba, *Spline models for observational data.* SIAM, 1990. 26, 27, 39

[54] P. Graven, "Smoothing noisy data with spline function: estimating the correct degree of smoothing by the method of generalized cross-validaton," *Number. Math.*, vol. 31, pp. 377–403, 1989. 26

[55] M. Poot, J. Portegies, N. Mooren, M. van Haren, M. van Meer, and T. Oomen, "Gaussian processes for advanced motion control," *IEEJ Journal of Industry Applications*, p. 21011492, 2022. 27

[56] C. K. Williams and C. E. Rasmussen, *Gaussian processes for machine learning.* MIT press Cambridge, MA, 2006, vol. 2, no. 3. 27, 28

[57] D. Duvenaud, "Automatic model construction with gaussian processes," Ph.D. dissertation, University of Cambridge, 2014. 28

[58] G. Pillonetto, F. Dinuzzo, T. Chen, G. De Nicolao, and L. Ljung, "Kernel methods in system identification, machine learning and function estimation: A survey," *Automatica*, vol. 50, no. 3, pp. 657–682, 2014. 28

[59] D. G. Duffy, *Green's functions with applications.* Chapman and Hall/CRC, 2015. 40